TM-72-1011-2

# TECHNICAL MEMORANDUM

## CAPABILITIES OF THE SKYLAB-A SPECTROMETER (S191) FOR REMOTE SENSING OF SURFACE TARGETS IN THE THERMAL-INFRARED SPECTRAL REGION

Bellcomm

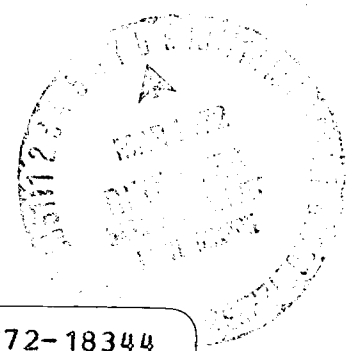

BELLCOMM, INC.
955 L'ENFANT PLAZA NORTH, S.W. WASHINGTON, D.C. 20024

## COVER SHEET FOR TECHNICAL MEMORANDUM

TITLE- Capabilities of the Skylab-A Spectrometer (S191) for Remote Sensing of Surface Targets in the Thermal-Infrared Spectral Region

TM-72-1011-2

DATE- January 20, 1972

FILING CASE NO(S)- 630

AUTHOR- R.W. Newsome, Jr.

FILING SUBJECT(S)-Earth Resources, Reststrahlen Spectral-Signatures, (ASSIGNED BY AUTHOR(S)- Infrared Spectrometer, Night-Time Targets, Xenon-Searchlight Beacon

ABSTRACT

This report reviews and demonstrates the effects of some of the factors which fundamentally limit the amount of information which can be deduced from spectrometer (S191) measurements, made from the orbital altitude of Skylab-A, of the thermal-infrared power radiated into space from typical surface targets. The particular significance of this spectral region is that the power radiated at night is comparable in intensity to that in daylight.

Calculations were made which simulate the quality of spectrometer data that could be expected from spectral measurements made in space, of the thermal-infrared radiation emitted from typical rocks on the surface. The results indicate that the reststrahlen structure in these spectra is not distinctive enough to permit reliable identification of the rocks. This conclusion is confirmed by relevant data which have already been obtained from aircraft and spacecraft.

Examples are also presented which show the potential significance of making thermal-infrared measurements at optimum times, during night or day, when the temperature contrast is greatest between the different constituents of a particular composite target. Detailed calculations show that thermal-infrared measurements, made by the spectrometer (S191) from Skylab-A, would not be impaired by radiation from a 20-kW xenon-arc searchlight, proposed for use as a target beacon which could be identified by an astronaut at night.

In a direct role, the spectrometer (S191) does not appear to be exceptionally useful for passive remote-sensing of surface targets in the thermal-infrared spectral region, because the spectral structure in the emissivity of these targets is usually not distinctive enough to permit identifications to be made reliably. In an indirect role, however, spectrometer measurements in this spectral region should be invaluable for determination of effects due to atmospheric absorption, and possibly for optimum selection of thermal-infrared channels for scanner imagery on future missions.

TABLE OF CONTENTS

TABLE OF CONTENTS (Cont'd.)

Bellcomm

955 L'Enfant Plaza North, S.W.
Washington, D. C. 20024

date: January 20, 1972

to: Distribution

TM-72-1011-2

from: R. W. Newsome, Jr.

subject: Capabilities of the Skylab-A Spectrometer (S191) for Remote Sensing of Surface Targets in the Thermal-Infrared Spectral Region - Case 630

TECHNICAL MEMORANDUM

## 1.0 INTRODUCTION

The capabilities of the infrared spectrometer (S191), for remote sensing at night or day in the thermal-infrared region of the electromagnetic spectrum, are examined from two points of view in this report. The first exercise involves a review of some factors which fundamentally limit the amount of information that can be obtained about surface targets from passive measurements made from space in this spectral region. The second exercise is directed to the specific question of whether or not spectrometer measurements would be impaired by thermal-infrared radiation from a visible searchlight beacon, proposed for use as a target marker which could be identified by an astronaut at night.(1)

The infrared spectrometer is sensitive to radiation from the ultraviolet end of the visible spectrum at 0.4μm to the near-infrared region at 2.4μm, and in the thermal infrared region from 6.2 to 15.5μm. Thermal-infrared radiation is absorbed by atmospheric water vapor and $CO_2$ to an extent which usually limits the use of this latter spectral region to the wavelength interval from ∿8 to ∿13μm for reception in space of radiation from surface targets.(2) The sensitivity of the spectrometer extends beyond this limited wavelength interval in order to facilitate measurements of the vertical profiles of atmospheric temperature and water vapor density.(3) With the exception of the ozone absorption band at ∿9.6μm, there is good transmission through the atmosphere for radiation with wavelengths between ∿8 and 13μm when there are no clouds or particulate hazes in the line-of-sight.

The intensity of thermal-infrared radiation emitted from surface targets at night, in the wavelength interval from 8 to 13μm, is comparable to that in daylight. One of the two reasons for this is that the diurnal variations of surface temperatures on Earth are small compared to the average temperature on the Kelvin scale. The other reason is that the spectral intensity of radiation from the sun at the orbital distance of the Earth is negligible compared to emission from the earth in this spectral interval.[2]

The infrared spectrometer (S191) measures the spectral power of the radiation which it receives. The power spectrum of radiation emitted from a body in thermal equilibrium is a function of the temperature of the body and of the spectral emissivity of its surface. These two variables are generally complicated functions of the microscopic and the macroscopic properties of the target.

The first part of this report contains a review of some fundamental problems associated with the extraction of values for temperature and spectral emissivity from field data. Several detailed examples are presented which show the usefulness and limitations of spectral signature identification based on reststrahlen structure in the spectral emissivities of some rocks and minerals. Reststrahlen signatures could in principle be used to remotely identify different types of silicate rocks. In practice, however, the potential of this approach is seriously curtailed due to atmospheric degradation and multiple scattering of radiation emitted from rough and powdery surfaces. Both of these effects are particularly serious because the reststrahlen spectral lines are typically broad and shallow for arbitrarily cut, unpolished crystals at room temperature.

The first section of this report also contains several examples which show that there are often optimum times during the day or night for temperature measurements via remote sensing of the thermal-infrared radiation from composite targets. This is due to the fact that materials with differences in thermal properties exhibit characteristic changes in their relative temperatures during the diurnal cycle. For example, substances with large thermal inertia are often easier to identify after sundown, because their temperatures remain high and result in an increase in the intensity of their emission spectra relative to that from cooler substances. Nevertheless, quantitative analyses of target properties, in terms of such time-dependent temperature information, are very difficult due to the complexity of surface, subsurface, and atmospheric boundary conditions in most field situations.

This first section is concluded with a brief summary of recent results from aircraft and spacecraft. The summary indicates that quantitative interpretation of target properties based on remotely sensed spectral data in the thermal-infrared region is marginal, except possibly in special cases. Additional aircraft flights appear to offer a relatively inexpensive way to determine how frequently these special cases will occur in practice, and how useful the results from them will be.

The second part of this report is addressed to a hypothetical problem associated with a proposed scheme which would permit the spectrometer (S191) to obtain data from selective surface targets at night.[1] Measurements at night are desirable complements to those made in daylight, because opportunities for target acquisition would be increased, and because diurnal variations in the relative intensity of emission spectra from the constituents of some targets may be easier to detect and interpret. This problem is developed as an educational exercise in order to provide physical insight into some of the performance specifications for the spectrometer in terms of its ability to make measurements of surface targets from space.

Target acquisition for the infrared spectrometer (S191) is completely controlled by an astronaut who must rely on visible light for illumination of the target. Data taken with the spectrometer at night would generally not be useful for identification of the radiative source, because neither the spectrometer or its viewfinder camera record images in the thermal-infrared spectral region.

Belz has shown that a 20-kW xenon-arc searchlight, currently in use at the Cape Kennedy launch pads, could provide a flashing signal suitable for easy recognition by an astronaut.[1] Specifically, he has shown that the intensity of a recognizable flashing signal at the altitude of Skylab A would be $\sim$1000 times above the threshold of the unaided human eye, for detection of this beacon against a background of the Earth illuminated by the full Moon.

Information in the open literature, about the radiance of the xenon-arc in the visible and near-infrared spectral regions, is used to deduce an upper limit for the spectral radiant intensity of thermal-infrared radiation in the searchlight beam. This beam intensity is compared with the spectral sensitivity of the spectrometer for a standard 1 sec scan of a surface target, when the measurement is made from the orbital altitude of Skylab A. The results show that the searchlight beam would not contaminate spectral measurements made in the atmospheric transmission window from 8 to 13$\mu$m, because the beam intensity at the altitude of Skylab A is less than the noise level of the spectrometer in this spectral interval.

## 2.0 REMOTE SENSING OF SURFACE TARGETS VIA DETECTION OF THERMAL-INFRARED RADIATION WITH S191

This chapter reviews some of the factors which fundamentally limit the uniqueness with which (S191) spectrometer measurements, made from Earth orbit in the thermal-infrared spectral region, can be used to deduce the temperature and spectral emissivity of surface targets. Also included is a brief discussion of what can be inferred about some targets whenever such measurements of temperature and/or spectral emissivity are successful. These fundamental considerations are followed by a summary of some representative field and laboratory measurements in order to gain some perspective about the potential usefulness of the spectrometer for remote sensing of Earth resources from space.

Refer to Appendix A for a description of the primary sub-systems of the spectrometer and a summary of relevant design specifications.[4-6]

### 2.1 Problems Associated with Unique Interpretation of Spectrometer Data

The infrared spectrometer (S191) measures the spectral power of the radiation which it receives. The intensity of the power which a perfect radiator emits at any specific wavelength can be uniquely related to the equilibrium temperature of the radiator by the Planck radiation function $N_\lambda(T)$. The emission spectrum for an imperfect radiator is defined as the product of the Planck function with an efficiency factor $\varepsilon_\lambda$, which is known as the spectral emissivity. The temperature dependence of the emissivity factor can usually be neglected for the range of temperature variations on the surface of the Earth.

At any fixed temperature, the radiated power predicted by the Planck function goes through a single maximum at a wavelength which is inversely proportional to the temperature. Measurements of radiated power made at wavelengths around this maximum can be used to determine the temperature of the emitter if spectral variations in emissivity are negligible. Temperature measurements become more difficult when the emissivity has a lot of spectral structure. On the other hand, this spectral modulation of the radiated energy may contain a great deal of information which can be utilized for identification of the target and some of its physical properties.

Let us now examine a mathematical expression which summarizes the functional dependence of spectral power in the thermal-infrared region which would be received from the Earth by the spectrometer in space. We will only consider the spectral interval between 8 and 13μm, and therefore the intensity of reflected solar radiation may be neglected with respect to thermal emission from the Earth.[2] The spectral power $[P_\lambda(\theta,t)]_j$ (in units of Watts/μm), which the spectrometer would measure at any time (t) of night or day when its field-of-view is completely filled by a homogeneous surface target (j) at an equilibrium temperature (T), may be represented by:

$$[P_\lambda(\theta,t)]_j = \{\tau_\lambda(\theta,t)[\varepsilon_\lambda(\theta,T,t)]_j N_\lambda[T(t)] + \phi_\lambda(\theta,t)\} \eta_\lambda(t) A_c \, d\Omega. \quad (1)$$

The first cluster of terms inside the curly brackets represents the radiative flux received by the spectrometer from the surface target when the line-of-sight makes an angle θ with the surface normal. The factor $[\varepsilon_\lambda(\theta,T,t)]_j$ represents the spectral emissivity of the $j^{th}$ target; $\tau_\lambda(\theta,t)$ represents the atmospheric transmission; and $N_\lambda(T)$ is the Planck radiation function in units of $Watts\text{-}cm^{-2}\text{-}sr^{-1}\text{-}\mu m^{-1}$. The second term in the curly brackets $\phi_\lambda(\theta,t)$ represents the radiative contribution from atmospheric emission. Note that when the atmospheric transmission $\tau_\lambda$ is close to unity, then Kirchhoff's law indicates that radiative contributions from the atmosphere will be of the order of $(1-\tau_\lambda)$. Under these conditions, the radiative term $\phi_\lambda$ is usually negligible with respect to the intensity of radiation from the surface of the Earth. The factors outside the curly brackets in Equation 1 represent: (a) the spectral efficiency $\eta_\lambda(t)$ of the total detection system at time (t); (b) the area $A_c$ of the spectrometer collection aperture; and (c) the solid angle dΩ of the acceptance cone of the spectrometer.

The primary objectives of spectrometer measurements of the spectral power $P_\lambda$, are to determine the target temperature (T) and/or the spectral emissivity $\varepsilon_\lambda(\theta,T,t)$. The spectrometer operator has limited control over the wavelength (λ), the angle (θ), and the time (t) at which measurements are made. A change in the value of any of these variables can in principle yield a

new relation via Equation 1 between the measured quantities $P_\lambda(\theta,t)$ and the unknown parameters (T) and $\varepsilon_\lambda(\theta,T,t)$. Unfortunately, this set of equations cannot be solved for (T) and $\varepsilon_\lambda(\theta,T,t)$ unless: (a) the emissivity and the temperature are constant for the entire group of spectral measurements; (b) the atmospheric transmission ($\tau_\lambda$) and radiative emission ($\phi_\lambda$) are known; and (c) the instrument efficiency $\eta_\lambda$ is known. The significance of in-situ ground-truth information about a target is that it can often be used to relax these constraints. For example, Equation 1 can be solved uniquely for $\varepsilon_\lambda(\theta,T,t)$ if the target temperature is known in addition to $\tau_\lambda$, $\phi_\lambda$, and $\eta_\lambda$. Conversely, if the emissivity of a particular target is known, then its temperature may be determined from spectrometer data.[7] Even in instances where ground-truth is not feasible, such as in planetary studies, a rough estimate of the target temperature is often sufficient to permit differential analyses of the observed power spectra which can be used to isolate spectral variations due to emissivity.[8]

Note that a primary objective of S191 measurements will be to determine the vertical temperature profile of the atmosphere and the vertical density profile of water vapor. Data for such atmospheric soundings will be acquired every time the spectrometer scans through the relatively opaque $CO_2$ bands around $\sim$15μm and the water vapor bands in the vicinity of $\sim$6.5μm.[3] These data should be invaluable for calculation of the atmospheric transmission $\tau_\lambda$ and radiative emission $\phi_\lambda$, because $CO_2$ and water vapor, in addition to ozone and particulate-haze, are the most important atmospheric absorbers of thermal-infrared radiation in the wavelength interval from $\sim$8 to $\sim$13μm.[2]

The emissivity may also be dependent upon polarization. Note, however, that a homogeneous target with a smooth surface cannot emit polarized radiation in a direction normal to the surface, because this would violate the unique symmetry of the configuration. The possibility of polarized emission at off-nadir angles is not indicated in Equation 1 because the spectrometer (S191) measures only the spectral power of the received radiation. The significance of this effective loss of information requires further study. Unfortunately, there appears to be a scarcity of data about the polarization of radiation emitted from typical Earth-resources targets in the spectral range from 8 to 13μm. Available tables show that the polarization of thermal-infrared radiation emitted from quiescent water, at angles smaller than $\sim$50° from the surface normal, is less than $\sim$6% over this

wavelength range.[9] Wire-grid gratings have been used to measure polarizations of thermal-infrared radiation which were as small as 1%.[10] Further study is, however, required to assess the feasibility and the desirability of spectral measurements of the polarization of radiation received by the spectrometer (S191).

Unique interpretation of remotely sensed data is made even more difficult by the fact that typical surface targets for Earth-resources applications are seldom homogeneous as indicated by Equation 1. Several types of objects may in general be scattered nonuniformly in the field-of-view. Furthermore, these objects may consist of inhomogeneously mixed substances with nonuniform properties which generally affect the overall spectral shape of the radiated power. The complexity of the composite power spectrum $P_\lambda$, which the spectrometer would receive from a target with (M) constituents, is represented by the following expression:

$$P_\lambda(\theta,t) = \left\{\tau_\lambda(\theta,t) \sum_{j=1}^{M} [\varepsilon_\lambda(\theta, T_j, t)]_j \, N_\lambda[T_j(t)][d\Omega(\theta)]_j + \right.$$

$$\left. + \phi_\lambda(\theta,t) \, d\Omega \right\} \eta_\lambda(t) \, A_c. \qquad (2)$$

Most of the symbols here are the same as those defined for use in Equation 1. A notable exception is the factor $d\Omega_j(\theta)$. It represents the effective solid angle which the $j^{th}$ constituent subtends at the spectrometer. An additional assumption in Equation 2 is that the emissivity and temperature of the $j^{th}$ constituent can be represented by the average values $[\varepsilon_\lambda]_j$, and $T_j$ respectively. There is little hope that all of the target parameters in Equation 2 could be determined solely from remote sensing measurements. Nevertheless, spectral and spatial measurements of the intensity of thermal-infrared radiation emitted from a composite target can provide useful diagnostic data when analyzed in conjunction with ground truth data, and with supplementary measurements made in other regions of the spectrum. Measurements should also be made at those times during the night or day when there is maximum contrast in temperature among the constituents of the target.

## 2.2 The Significance of Reststrahlen Signatures for the Identification of Rocks and Minerals

Many rocks and minerals have emissivities with more spectral structure in the thermal-infrared spectral region than at shorter wavelengths. This is in direct contrast to the spectral emissivities of vegetation and water, which exhibit relatively little information in the form of spectral structure in the wavelength interval from 8 to 14μm.[11]

Variations in spectral structure produced by the interaction of thermal-infrared radiation with rocks and minerals are referred too as reststrahlen (i.e., residual ray) phenomena. This structure appears at characteristic wavelengths in the form of minima in emission spectra and maxima in reflection spectra.[12] These spectral variations are due to resonant interactions between the radiation field and the fundamental lattice vibrations of the functional anion groups in the crystal. Distinct spectral structure due to reststrahlen phenomena occur at wavelengths of: (a) ∿7μm for rocks with carbonate anion groups; (b) ∿8.1μm for nitrites; (c) ∿7.25μm for nitrates; (d) ∿9.5μm for phosphates; (e) ∿8.85μm for sulphates; and (f) ∿9-11 and ∿18-25μm for all silicates.[13,14]

Identification of silicate materials is relevant for study of the surface geology of the Earth because they represent approximately 60% of the bulk volume of the surface crust.[15] Igneous rocks are in fact classified on the basis of their content of $SiO_2$, which is considered to be the "acidic" oxide in these materials.[16] For example, the $SiO_2$ content is: (a) less than 45% for ultrabasic rocks such as dunite; (b) between 45% and 53% for basic rocks such as basalt; (c) between 53% and 65% for intermediate rocks such as syenite; and (d) more than 65% for "acidic" rocks such as granite.[13,16] In general, basic rocks are rich in ferromagnetic materials, while acidic rocks are richer in light minerals such as quartz and feldspar.

The reststrahlen bands in silicate materials are due to fundamental vibrational frequencies of the tetrahedral Si-0 bond.[14,17] These resonant frequencies are characteristically modified by the presence of metallic atoms at the secondary coordinating positions in the lattice network. This effect is illustrated by the shift in the position of the reststrahlen

minima in the emissivity curves in Figure 1, from ∿9μm for "acid" rocks to ∿11μm for ultrabasic rocks. In principle, these spectral signatures provide a means of distinguishing between iron silicates (e.g., basalts) and aluminosilicates (i.e., "acid" rocks such as granite).[14]

Unfortunately, the reststrahlen structure in the emissivity of all rocks is degraded by surface roughness, and is almost totally eliminated when rocks are powdered to particle sizes with dimensions comparable to the wavelength of the emitted radiation (i.e., ∿10μm in the thermal-infrared region).[13,16] This behavior is due to the increased amount of multiple scattering which the emitted radiation must undergo in order to leave a rough surface or powdered medium. Complex mathematical models have been developed to describe this diffusion process, but the utility of such models for quantitative analyses of field data remains unproven.[18,19]

A selection of laboratory measurements of the spectral emissivities of several rocks and sands is contained in Figure 2. Note the relatively severe degradation of the reststrahlen spectra of quartz in the form of powder, sand or a rough-faced crystal, as compared to that for a large selectively-cut crystal with a polished face. The polished crystals obviously show the most distinct reststrahlen structure. Unfortunately, it is extremely unlikely that they ever occur in nature with polished faces of optimum cleavage. In the legend of Figure 2, the terminology Z-cut refers to a crystalline face cut perpendicularly to the optic axis, whereas X-cut refers to a face cut parallel to the optic axis and perpendicularly to one of the two-fold axes of symmetry.[20]

The spectral emissivity data in Figure 2 were obtained from measurements made in a laboratory by Lyon.[13] The samples were small and they were heated a few hundred degrees above room temperature in order to overcome the background of thermal emission from the spectrometer used to make the measurements. Lyon states in his report that there are calibration errors in the magnitudes of his spectral measurements with powdered samples. This statement is based on his conviction that there were undoubtedly temperature gradients in the heated powders.[13] It is therefore of interest to compare his results with the reflectance measurements by Hovis et al., because these latter measurements required minimum heating of the specimens.[16] For an opaque medium, the total reflectance coefficient $\rho_\lambda$ and the spectral absorptance coefficient $\alpha_\lambda$ are related by the equation,

$$\rho_\lambda + \alpha_\lambda = 1. \quad (3)$$

This equation is merely a statement of conservation of energy for radiation falling on a medium with zero transmittance. For a medium in temperature equilibrium, Kirchhoff's law states that the spectral absorptance $\alpha_\lambda$ is equal to the emissivity $\varepsilon_\lambda$, and therefore,

$$\rho_\lambda + \varepsilon_\lambda = 1. \quad (4)$$

The emissivity $\varepsilon_\lambda$ is generally a function of the angle of emittance. Similarly, the reflectance $\rho_\lambda$ is generally dependent on the corresponding angle of incidence or reflectance, with the other related angles averaged over the hemisphere. Fortunately, both Lyon[13] and Hovis et al.[16] appear to have made their measurements at angles near the surface normal. When Equation 4 is used to compare their data for quartz, one finds very good agreement in spectral shape and reasonably quantitative agreement in magnitude. For example, the emissivity obtained by Lyon, for quartz particles of $\sim$10μm diameter, confirms the anomalous secondary reflectance peak which Hovis et al. observed when the particle sizes were less than $\sim$38μm in their quartz sample.

In Figure 3, the spectral emissivity data $\varepsilon_\lambda$ from Figure 2 is multiplied by the Planck radiation function $N_\lambda(T)$ for a temperature of T=288°K. This is the average temperature of the surface of the Earth, and the product $\varepsilon_\lambda N_\lambda$ gives the approximate spectral intensity of radiation emitted by each of the five entries in Figure 3. The accuracy with which the spectrometer (S191) could resolve these spectral variations in intensity is indicated by the vertical error bars on the data points for the quartz powder. The lengths of these error bars represent $\pm$ NESR (i.e., noise-equivalent-spectral-radiance) obtained from the EREP Users Handbook.[5] The concept NESR is explained in Appendix D.

In Figure 4, the spectra in Figure 3 are multiplied by the atmospheric transmission $\tau_\lambda$ for a vertical path between the Earth and space.[2] Average values were used for the vertical profiles of the primary atmospheric absorbers, and

attenuation due to atmospheric haze was neglected. Note that the effective sea level path length for water vapor was obtained by integration of a representative vertical density profile for a temperate zone in winter.[2] The effective path length in summer is typically double that in winter.[21] The corresponding value for the transmission in summer may therefore be roughly estimated by squaring the value used in winter. The atmospheric transmission tables formulated by Hudson,[21] for water vapor and $CO_2$ were used to obtain the spectral transmission $\tau_\lambda$ for the effective absorption path-lengths which are listed in the caption of Figure 4. Ozone absorption was roughly estimated by a single average value.[2,21] The spectral resolution of these tables is equal to 0.1μm. This is equal to the resolution of the emissivity data obtained by Lyon,[13] and is also essentially equal to the spectral resolution of the spectrometer (S191) in this wavelength interval.[5]

Unfortunately, the inherent widths of the structure in reststrahlen spectra do not appear to be small compared to 0.1μm.[17] For example, the full width at half minimum of a typical reststrahlen line in quartz was observed to be only ∿0.07μm at the extremely low temperature of ∿4°K.[20] This indicates that an increase in the spectral resolution of the spectrometer (S191) would result primarily in increased resolution of the fine structure of spectral lines due to atmospheric absorption and emission. This would of course be helpful for correcting atmospheric distortion of reststrahlen spectra, but it is doubtful that a significant gain in the ability to identify these relatively broad spectra would be realized.

The spectra in Figure 4 represent approximations to the spectral distribution of radiant intensity which arrives at the spectrometer in space if the field-of-view is completely filled by only one constituent at a time. In practical situations there will generally be many types of materials simultaneously in the field-of-view of the spectrometer, as indicated by Equation 2. Unfortunately, reststrahlen minima in field rocks are typically broad and shallow because such rocks have rough surfaces and are often accompanied by fragmented sands of various sizes. Figure 5 contains a curve which illustrates how quickly reststrahlen spectra can be

washed out when the field-of-view of the spectrometer contains several materials. Each of the five spectra in Figure 4 were averaged together with equal weight to produce the composite curve in Figure 5. The spectral information which this composite curve exhibits about the target materials may be readily estimated by comparison with the radiance curve for a perfect emitter at the same target temperature, which also appears in Figure 5. The lengths of the error bars on this curve represent the change in spectral power that would be observed in space if the temperature of a perfect emitter on the surface were changed by an amount $\pm 1°K$ about an average value of 288°K. The first derivative of the Planck function $\partial N_\lambda(T=288°K)/\partial T$ was obtained from tables by Pivovonsky et al.[22] It is apparent that the only reststrahlen feature which the spectrometer (S191) could reliably detect would be the small decrease in radiance from $\sim 8.5$ to $\sim 9.3\mu m$ (corresponding to an effective decrease in apparent temperature of $\sim 2°K$) compared with the radiance in the wavelength interval from $\sim 10$ to $\sim 12.5\mu m$. This is due to the relatively large amount of $SiO_2$ in the material of the composite target which was used in this example.

The general blandness of the effects predicted in Figures 4 and 5 is confirmed by the satellite data in Figure 6, which compare spectra taken over deserts (i.e., $SiO_2$) with that taken over water. These data were obtained on Nimbus 3 and 4 by the Michelson interferometers IRIS B and D respectively. Note that the radiance data in Figures 3, 4, and 5 are in units of intensity $N_\lambda$, plotted as a function of wavelength $\lambda$ with the incremental wavelength intervals $\delta\lambda$ held constant. The data in Figure 6a, however, are in units of intensity $N_\nu$, plotted as a function of <u>inverse</u> wavelength (i.e., $\nu \equiv 1/\lambda$) with the incremental intervals in inverse wavelength ($\delta\nu$) held constant. A quantitative comparison of the relative shapes of these spectra may be made by multiplying data with units of $N_\nu$, by the factor ($|\frac{\delta\nu}{\delta\lambda}| = 1/\lambda^2$) in order to transform to the same spectral baseline used for $N_\lambda$.

The data in Figures 4 through 6, indicate that reststrahlen spectral signatures are not very distinctive under actual field conditions. Note, however, that if the materials in a composite target have significantly different thermal properties, then reststrahlen signature identification may be more helpful if the measurements are made at those times during the diurnal cycle when temperature contrasts among the individual target constituents are greatest. Several examples of the time dependence of diurnal variations in the relative temperature of materials with different thermal properties are illustrated in the following section.

## 2.3 The Significance of Temperature Measurements Made at Selected Times of Night or Day

The temperature dependence of the spectral power radiated from surface targets is contained in the Planck function $N_\lambda(T)$. As noted earlier, variations from the average surface temperature of the Earth are usually small enough so that one may neglect the intrinsic temperature dependence of the emissivity factor $\varepsilon_\lambda$. The emissivity is the correctional factor which is multiplied with the Planck function in Equations 1 and 2 in order to describe the spectral power emitted from non-ideal radiators. The Planck function describes the spectral power radiated from a perfect blackbody at an equilibrium temperature T, and the formula for this function may be expressed as:

$$N_\lambda(T) = \left(\frac{2hc^2}{\lambda^5}\right) \frac{1}{e^{hc/\lambda kT}-1} \quad \text{Watts/cm}^2\text{-ster-}\mu\text{m}, \qquad (5)$$

where c is the velocity of light, $\lambda$ is the wavelength, and h and k respectively represent the Planck and Boltzmann constants.[21]

The temperature of a surface target at any instant of time is generally a complicated function of: (a) the density, and the thermal properties of the target (i.e., conductivity and thermal heat capacity); (b) the spectral emissivity, (which is the efficiency factor for radiative transfer of energy to and from the target); (c) variations in the intensity of solar radiation at the target (e.g., due to cloud cover as well as seasonal and daily changes in sun angle); and (d) thermal boundary conditions which determine the conductive and convective flow of energy between the target and its terrestrial environment. Some of these parameters can be related to more specific characteristics of the target such as porosity, moisture content, surface roughness, etc.

The partial differential equations, which describe the relation between heat flow and the time-dependent temperature of a body, may be readily solved when the thermal boundary conditions are not overly pathological. Illustrations of such solutions are contained in Figure 7a.[23] The curves in this Figure represent predictions of diurnal variations of temperatures in summer of several types of rocks found at the Mill Creek, Oklahoma test site. Specifically, the rock types are:

(a) granite, (an igneous rock with typically ∿70% $SiO_2$ and ∿14% $Al_2O_3$)[24]; (b) limestone, (a sedimentary rock composed primarily of calcium carbonate with typically ∿43% CaO, ∿42% $CO_2$, ∿8% MgO, and ∿5% $SiO_2$)[25]; and (c) dolomite (a modified limestone composed of magnesium and calcium carbonates [Ca, Mg $(CO_3)$], with a relative composition by weight of typically ∿22% MgO, ∿30% CaO, and ∿48% $CO_2$).[25]

The curves in Figure 7a show that the largest temperature difference between granite, limestone, and dolomite occur during the predawn hour of 6:00 A.M. The dolomite remains warmer than either the limestone or the granite because it has the largest thermal inertia.[23] Under normal conditions, the thermal contrast between materials with different thermal inertia is largest at dawn. On the other hand, materials with the same thermal inertia, but with differences in albedo, show greatest temperature contrast during the day when they are heated by the sun.[23]

From Figure 7a, the predicted difference in temperature between dolomite and granite is ∿12°K at 6:00 A.M. If the emissivities of these two rocks were identical, then the ratios of the spectral intensities of radiation emitted from them would be equal to the ratios of the Planck functions at their respective temperatures. For example, the temperature of the dolomite at this instance in time is ∿301°K and that of the granite is ∿289°K. The ratio of the corresponding Planck functions (i.e., $N_\lambda(301°K)/N_\lambda(289°K)$ is equal to 1.2 for $\lambda$=11μm and 1.25 for $\lambda$=9μm.[9,22] For a target composed of both dolomite and granite, one might therefore expect to have a better chance of detecting reststrahlen features due to emission from the dolomite if the measurements are made during the pre-dawn hours. Unfortunately, the primary reststrahlen line in dolomite occurs at 6.45μm where atmospheric absorption by water vapor is very high. Dolomite also has a very weak reststrahlen line in its emissivity at 11.20μm.[13] Unfortunately, this reststrahlen dip is only ∿1% in magnitude and the corresponding change in the spectral radiance at a temperature of ∿300°K is slightly less than the noise level (i.e., NESR) for S191. It is also of interest to note that limestone, composed of pure calcite (i.e., $CaCo_3$) has a strong reststrahlen minimum at 6.7μm and a weaker dip at 11.3μm. Aragonite is an unstable form of calcite[25] which also has a strong reststrahlen dip at 6.7μm, but the weak secondary line occurs at 11.5μm.[13] Any attempt to make field measurements of those reststrahlen features which lie within the atmospheric transmission window between 8

and 13μm would have run into additional trouble at the Mill Creek test site, because ∿70% of the rocks there were covered with lichens and moss.[23]

The diurnal temperature curves in Figure 7b show that water retains heat at night much more effectively than typical agricultural vegetation.[26] In direct contrast to this, note that the high rate of evaporation of the excess moisture which accumulates in fault and fracture zones makes them cooler at dawn than the surrounding ground.

The curves in Figures 7a and 7b are obviously idealizations which neglect practical problems such as: (a) the past history of abrupt changes in the temperature of the atmospheric interface[23]; (b) variations in moisture and in cover due to soil and/or vegetation[27]; and (c) the inhomogeneity of the vegetation and/or rocks. Such factors obviously interfere with the ultimate goal of establishing unique relationships between the temperature, and the physical and environmental characteristics of targets. In most cases, this goal cannot be realized, even when ground-truth data are available to limit the number of unknown parameters in the theoretical models used to predict the temperature, as a function of values for the physical parameters of the target. As noted in the following section, however, thermal imagery with very broad spectral resolution has more than proven its worth for night-time detection of thermal anomalies associated with inhomogeneities in the physical properties of targets.[28,29] There is therefore hope that improvements in the spectral and spatial resolution of remote-sensing measurements, made at appropriate times during the diurnal cycle, may yield quantitative information about some types of heterogeneous targets.

On the other hand, the spectral intensity of thermal-infrared emission from relatively homogeneous targets, such as the oceans, can often be interpreted directly in terms of an effective target temperature. This is because "ground truth" measurements can be reliably used to correct for the effects of emissivity. For example, calculations in a recent report indicate that thermal-infrared measurements made in space can be used to deduce the effective surface temperatures of the oceans to an accuracy of ∿0.15°C, if the data are taken over specific wavelength intervals which permit effective corrections to be made for absorption by the atmosphere.[30] But even for this apparently simple type of target, there is no simple relation between the effective temperature which is deduced and the temperature profile of the upper levels of the ocean.

The primary problem is that the penetration depth of thermal-infrared radiation in the ocean is only $\sim$0.01 cm[31], and this thin film is generally not in temperature equilibrium with the water below it.[32]

## 2.4 The Outlook for Remote Sensing with Thermal-Infrared Radiation as Seen from the Perspective of Some Past Results

This sub-section is introduced with a brief discussion of some results obtained with multispectral scanners because these instruments are essentially spatial-imaging spectrometers with relatively poor spectral resolution. Scanner imagery with poor spectral resolution in the thermal-infrared region has produced some very impressive and useful information about Earth-Resources targets. One of the primary reasons for this is that the output data is pictorial and it may be interpreted directly in terms of topographic temperature and/or emissive profiles of the actual scene.

In spite of relatively poor spectral resolution, scanner measurements at night have clearly illustrated temperature contrasts caused by differences in the rates of the diurnal flow of heat from materials with different thermal properties.[28,29,33] For example, thermal-infrared imagery, which were taken on aircraft flights over the San Andreas fault, gave better contrast definition of the fault at night than in daylight.[34,35] Aircraft flights at night have also been used to obtain thermal-infrared imagery which show promise of expediting other types of surveys, such as: (a) identification of different types of rocks;[23,27,36] (b) location of surface salt domes which may be associated with oil deposits in deserts;[37] and (c) study of hot springs fumaroles, and volcanoes.[38]

Meteorological satellites have also been used to obtain scanner imagery from space in the thermal-infrared region of the spectrum.[39] In general, however, this imagery has had relatively poor spatial resolution, because the primary objective of these satellites was to survey the atmosphere over large areas of the globe. Reliable interpretation of surface imagery obtained from most meterological satellites is therefore limited to regions with uniform emissivity over large areas, such as the oceans and deserts. For example, data from the thermal-infrared channel (10.5-12.5$\mu$m) of the scanning radiometer on ITOS-1 (Improved Operational TIROS Satellite-1) have been used to produce thermal maps of the ocean with an accuracy of $\sim$1°C over spatial resolution elements of 7.4 km in diameter.[40]

The capabilities of the filter wedge spectrometer (S191), for measurements of surface targets from Skylab-A, are similar (with the possible exception of system noise) to those of two types of spectrometers flown on aircraft.[41,42] This fact is evident from the comparisons in Table 1. The table also contains relevant information about the two Michelson interferometers, IRIS B and D, which were respectively flown on Nimbus 3 and 4.[43-45] With the exception of spatial resolution, these instruments had flight capabilities which are comparable to those projected for S191 aboard Skylab-A.

The data, in the first line below the entry for S191 in Table 1, summarize the measurement capabilities of the spectrometer flown by Hovis et al.[41] These investigators measured spectra, over relatively homogeneous desert terrain, from altitudes which ranged between 0.7 and 10km. The reststrahlen dip due to $SiO_2$ was barely visible at the lowest altitude, and was almost completely washed out at the highest altitude due to attenuation of the upwelling radiation by atmospheric ozone and haze. Their poor results are discouraging, but nevertheless consistent with conclusions based on calculations presented earlier in this report.

The data, in the second line below the entry for S191 in Table 1, summarize the measurement capabilities of the spectrometer flown by Lyon et al.[42] These investigators emphasized the importance of high spatial resolution in order to obtain high quality spectra from rock and mineral fields. As shown in Table 1, the time required for a complete spectral scan by their instrument was 180 times faster than the scan time of the instrument used by Hovis et al.[41] Spectral signatures of some igneous rocks were identified by Lyon et al.[42] at the relatively low altitude of 2.74 km, but the information to noise ratio was marginal. These data would have been degraded further if measurements had been made at higher altitudes. Unfortunately, neither the paper by Lyon et al.[42] or the one by Hovis et al.[41] specifies the sensitivity of their instrument in terms of noise-equivalent-spectral-radiance.

The last two entries in Table 1 summarize the measurement capabilities of the interferometers flown on the meteorological satellites, Nimbus 3 and 4.[43-45] Both of these papers contain a comparison of a spectrum of the thermal-infrared

radiance measured over the Sahara desert with a similar type of spectrum measured over the Mediterranean Sea. The desert sand is primarily $SiO_2$. The emissivity data for quartz sand in Figure 4 indicate that only a relatively flat depression in the vicinity of ∿9μm should be expected in the spectra taken over the desert. As shown in Figure 6, what is actually observed is that the average intensity of radiation in the atmospheric transmission window from ∿8 to ∿9.3μm, is almost uniformly reduced by ∿10°K below that of the intensity from ∿10.3 to ∿13μm, which is the transmission window on the other side of the ozone absorption band. This effect is not observed for spectra taken over the sea. Unfortunately, all of the detailed spectral structure in these data appear to be due to atmospheric effects. These results are similar to those in the example illustrated in Figure 5.

The data which have been presented in this report indicate that reststrahlen spectral structure offers only marginal possibilities for remote identification of surface rocks and minerals when their thermal-infrared emission spectra are measured from aircraft or spacecraft. Additional test flights on aircraft offer a highly desirable and economic way to either confirm these reservations or to establish realistic goals for future measurements from space.[46]

As mentioned earlier, there is no question about the potential importance of spectrometer (S191) measurements, made from Skylab A, for determination of vertical temperature profiles in the atmosphere and for determination of the vertical density profiles of water vapor and ozone.[3,45] These profiles will be invaluable for calculation of the atmospheric transmission $\tau_\lambda$, and emission $\phi_\lambda$ which appear in Equations 1 and 2. Precise knowledge of these two factors would also permit corrections for atmospheric transmission to be made accurately, on data taken with the multispectral camera (S190) and scanner (S192).

Spectrometer measurement with good spectral resolution are also potentially valuable for future selection of scanner channels, whose locations and widths are to be tailored to maximize the receipt of spectral and spatial information about specific types of targets. The spectral characteristics of such arrays of optimized scanner channels will generally be time-dependent. Therefore, spectrometer measurement to determine these spectral characteristics will generally be desirable at night as well as in daylight. The feasibility and desirability of making such measurements from spacecraft, should always be tested initially from aircraft and/or balloon platforms.

## 3.0 THE FEASIBILITY OF REMOTE SENSING OF SURFACE TARGETS AT NIGHT BY S191 WHEN IT IS IN THE BEAM OF A TARGET ACQUISITION BEACON

As previously noted in the introduction to this report, Belz has shown that an astronaut on Skylab-A should be able to detect with unaided vision, the radiation from a 20-kW xenon-arc searchlight when the spacecraft is in its beam.[1] This section contains calculations which show that the maximum possible intensity of thermal-infrared radiation in the beam of the proposed searchlight, would not be detectable by S191 from the orbital altitude of Skylab-A at 435 km. Several relevant fundamentals of radiometry are also reviewed here.

### 3.1 The Average Spectral Intensity of Thermal-Infrared Radiation Emitted from Typical Surface Targets

This sub-section reviews the basic radiometric procedure for calculation of the average spectral intensity of thermal-infrared radiation emitted from typical surface targets on Earth. Three fundamental approximations are used to characterize these targets. The first approximation is the assumption of an average equilibrium surface temperature of 288°K. The second is that of unit surface emissivity over the thermal-infrared spectral range. With the exception of emissivity dips to ∿60% at reststrahlen bands for some minerals and rocks, this approximation is usually valid to within ∿10% for most surface targets of natural origin.[11,13,16,31,33] The third of these approximations is that the emitting surface is perfectly diffuse (i.e., Lambertian). This is a very reasonable assumption because many ground targets related to Earth Resources Applications have numerous unresolved small-scale structures with random surface orientations (e.g., leaves, soil particles, etc.)

As noted in Appendix A, the field-of-view of the spectrometer (S191) is fixed at one milliradian. The diameter of the corresponding surface resolution element is 0.435 km, when viewed from nadir at the Skylab altitude of 435 km. Larger surface-target areas will be subtended for off-nadir viewing angles which do not include the horizon in the fixed field-of-view. It is shown in Appendix B, however, that the spectral power received from a Lambertian surface which always fills a fixed field-of-view is independent of the viewing angle if differences in atmospheric transmission are neglected. The field-of-view of the spectrometer aperture is small enough so that variations from the average angle subtended by the target may be neglected. In this small-angle approximation, the spectral power which the spectrometer would receive in space from the surface of the Earth, is:

$$P_\lambda^C(\text{Earth}) = \tau_\lambda(\theta) \left(\frac{A_c}{R(\theta)^2}\right) A_s(\theta) N_\lambda(288°K) \cos\theta \quad \text{Watts}/\mu m, \qquad (6)$$

where $\tau_\lambda(\theta)$ is the atmospheric transmission along the path of length $R(\theta)$, which makes an angle $\theta$ with the local vertical at the target; $A_c$ is the area of the acceptance aperture of the spectrometer; $A_s(\theta)$ is the area subtended by the target at angle $\theta$; and $N_\lambda(288°K)$ represents the Planck radiation function in units of Watts-cm$^{-2}$-ster$^{-2}$-$\mu$m$^{-1}$ at a temperature of 288°K. The function $\cos(\theta)$ represents the angular dependence in the intensity of radiation emitted from a Lambertian surface at an angle $\theta$ from the local vertical.[31] In Appendix B and Figure 9, it is shown that the source area may be expressed as:

$$A_s(\theta) \cong \pi\delta^2 R(\theta)^2/(4\cos\theta) \qquad (7)$$

where $\delta$ is the full angular field-of-view.

The product of the last three factors in Equation 6 represents the source strength, and it is defined as the spectral radiant intensity:

$$J_\lambda(\text{Earth}) \equiv A_s(\theta) \cos(\theta) N_\lambda(288°K) \quad \text{Watts-ster}^{-1}\text{-}\mu m^{-1}. \qquad (8)$$

Note that the other terms from Equation 6, [i.e., $\tau_\lambda(\theta) A_c/R(\theta)^2$] are <u>independent</u> of the characteristics of the radiant source. Tables of the Planck function[9] were used to calculate the spectral radiant intensity $J_\lambda(\text{Earth})$ which is plotted in Figure 8.

### 3.2 <u>The Spectral Radiant Intensity in the Beam of the Searchlight</u>

This aspect of the problem would be trivial if the intensity of the searchlight beam were known as a function of divergence-angle and wavelength, in the thermal-infrared region of the spectrum. Unfortunately, this information does not appear to be available in the open literature. Therefore, an attempt was made to deduce estimates of these performance characteristics from available information about the searchlight parameters. The results are summarized briefly in this sub-section, and the procedures used to obtain them are discussed at length in Appendix C.

The xenon-arc searchlight, which Belz[1] suggested for use as a target beacon, is schematically drawn in Figure 10. The xenon-arc is enclosed in a quartz envelope and it is located at the focal point of a paraboloidal reflector.[47] This arc radiates ∿50% of the 20-kW input power to the lamp.[48-50] The cathode hot-spot of the arc has a maximum brightness of 6,875 candles/mm$^2$[47], and in Appendix C this is shown to be equivalent to a blackbody temperature of 8,070°K. With the exception of deviations due to pressure-broadened line structure around 0.9μm and in the ultra-violet spectral region, the average spectral irradiance of the arc out to 2μm can be adequately represented by a blackbody spectrum at a temperature of ∿6000°K. This is discussed in Appendix C and illustrated in Figure 11.

The source of thermal-infrared radiation in the searchlight is the quartz envelope which contains the xenon gas. The reason is that this envelope, of ∿5mm thickness, is opaque to radiation over the wavelength range between ∿4 and 50μm.[21,51,52] As noted in Appendix C, it is difficult to estimate the steady state temperature of this envelope, however, an upper limit is obviously set by the softening temperature of quartz at ∿1800°K.[31]

Let us now estimate the far-field intensity of the beam from the searchlight in Figure 10. For simplicity, we assume that the source is spherical with area (A), and that it has a Lambertian surface with unit emissivity. Under these conditions, the spectral radiant intensity ($J_\lambda$) averaged over the beam-width far from the reflector, is approximately:

$$J_\lambda = (\Omega_R/4\pi)(\pi A)N_\lambda(T)/\Omega_B \quad \text{Watts-ster}^{-1}\text{-}\mu\text{m}^{-1}, \qquad (9)$$

where $N_\lambda(T)$ is the Planck radiation function in units of Watts-cm$^{-2}$-ster$^{-1}$-μm$^{-1}$; and $\Omega_B$ and $\Omega_R$ respectively represent the solid angle of the beam and the solid angle subtended by the reflector at the source. In this equation, the product $(\pi A)\ N_\lambda(T)$ represents the total spectral power emitted by the source into the full spherical solid angle; while the factor $(\Omega_R/4\pi)$ represents the fraction of this spectral power which is received by the reflector and focused into the solid angle of the beam ($\Omega_B$). From Figure 10 it follows that $\Omega_R \tilde{\approx} 2\pi$, and that:

$$\Omega_B \approx \pi r^2/\ell^2 \equiv \pi\alpha^2, \qquad (10)$$

where (r) is the source radius; ($\alpha$) is the half-angle of the beam divergence; and the average source to reflector distance is $\ell$. For the particular paraboliodal reflector in Figure 10, this average distance is approximately 3/2 times the focal length (f). Substitution of this information into Equation 9 yields the following equation for the spectral radiant intensity of our searchlight:

$$J_\lambda \cong \frac{9}{2}\pi f^2 N_\lambda(T) \qquad \text{Watts-ster}^{-1}\text{-}\mu\text{m}^{-1} . \qquad (11)$$

This result, which is based on a first-order approximation for the focal properties of a paraboloid, is a function of the source temperature but it is independent of the source size. It follows, therefore, that the spectral radiant intensity in the beam is independent of the total power radiated if the source is held at constant temperature. As noted in Appendix C, this general conclusion is rigorously correct because the alternative condition would violate the second law of thermodynamics. Appendix C also contains a pragmatic check of the quantitative validity of Equation 11. This check was made by calculating the visible brightness of the beam with the aid of Equation 11, and comparing the result with the reported performance data for the searchlight. The agreement obtained in this comparison was very good.

Upper limits to the spectral radiant intensity in the beam of the 20-kW xenon-arc searchlight were calculated with the aid of Equation 11, and the results are plotted in Figure 8. For wavelengths less than 2$\mu$m, the data in Figure 11 indicate that the average spectral characteristics are adequately approximated by a blackbody temperature of 6,000°K. A curve corresponding to a source temperature of 8000°K is included in Figure 8 for comparison. The transmission through the quartz envelope is ~93% over this wavelength range, and this small correction was not included in Figure 8. As noted earlier, the quartz envelope is an opaque source of radiation for wavelengths between ~4 and ~50$\mu$m. A conservative upper limit for the beam intensity in this spectral region was obtained on the basis of two assumptions. One was the use of the softening temperature of quartz, which is 1800°K. The other was that there were no degradations in beam intensity due to aberrations caused by the relatively large displacement of the source material from focal point of the paraboloidal reflector. The procedure used to estimate the

emissivity of the quartz over this spectral range is discussed in Appendix C. Note that the use of the maximum value of unity would not have affected the conclusion obtained from the final comparison of spectral radiant intensities.

Figure 8 also contains a curve of the spectral radiant intensity that would be produced if 20-kW of power were radiated upward from a completely opaque lid with a Lambertian surface which is just big enough to cover the top of the searchlight reflector. The temperature of this lid must be a minimum of 1700°K in order to radiate 20-kW from this surface area. It is apparent from Figure 8 that the spectral radiant intensity from such unfocused sources would be relatively weak in comparison with the spectral intensity of the focused searchlight beam.

### 3.3 The Change in Spectral Radiant Intensity Due to a Change in Target Temperature of NEΔT

The noise-equivalent-temperature-difference (NEΔT) is defined as that change in target temperature which causes the power received, at the input of a detection system, to change enough to produce an rms signal voltage at the system output which is equal to the corresponding rms noise voltage at this particular power level. In this sub-section, the NEΔT specifications for S191[4] are used to calculate the corresponding change in spectral radiant intensity, and this is compared with the spectral intensity in the beam of the searchlight.

Differentiation of Equation 6 with respect to temperature produces the following equation:

$$\delta P_{\lambda}^{C} = \tau_{\lambda}(\theta) \frac{A_c}{R(\theta)^2} A_s(\theta) \cos\theta \left[\frac{\partial N_{\lambda}(288°K)}{\partial T}\right] \delta T \quad \text{Watts}/\mu\text{m}. \qquad (12)$$

This equation relates the change in the spectral power received by the detector ($\delta P_{\lambda}^{C}$) with the corresponding change in the target temperature ($\delta T$). The differential change in temperature ($\delta T$) is defined as NEΔT when the change in spectral power at the collector ($\delta P_{\lambda}^{C}$) produces an output signal-to-noise ratio of unity. Under these conditions, this change in spectral power at the input is defined as the noise-equivalent-power (i.e., $NEP_{\lambda}$). The corresponding spectral radiant intensity from the target, at the vertical angle $\theta = 0$, is:

$$\delta J_\lambda = A_s \frac{\partial N_\lambda (288°K)}{\partial T} \delta T \quad \text{Watts-ster}^{-1}\text{-}\mu\text{m}^{-1} \quad . \qquad (13)$$

This expression is evaluated[22] and plotted in Figure 8 for $\delta T$ values of 0.1°K and 1°K, because they correspond to the tentative range of NE$\Delta$T in the original specifications for S191.[4] The recently released data of noise-equivalent-spectral-radiance[5] for S191 (i.e., NESR, which is defined in Appendix D), correspond to a value of $\sim$1°K for NE$\Delta$T from $\sim$8 to $\sim$13$\mu$m. For the sake of generality, these specifications for NE$\Delta$T do not include the correction due to degradation in atmospheric transmission. As shown in Appendix D, this correction can be made by dividing the uncorrected value of NE$\Delta$T by the atmospheric transmission along the path (i.e., $\tau_\lambda$). For a vertical path through the atmosphere in clear weather, the correction factor $(1/\tau_\lambda)$ is not much larger than unity over that part of the spectral region from $\sim$8 to $\sim$13$\mu$m which excludes the ozone absorption band.

In Figure 8, note that for wavelengths greater than $\sim$7$\mu$m, the spectral radiant intensity of the searchlight beam is less than that produced by a change of 0.1°K in the temperature of a surface target viewed from nadir by S191. This means that thermal-infrared radiation from the searchlight would, for all practical considerations, be undetectable by S191 from Skylab-A, even if the searchlight tracked the spacecraft continuously during one complete spectral scan (i.e., $\sim$1 sec).

It is of interest to note that if the xenon-arc had no quartz envelope, then the intensity of our searchlight beam, for wavelengths greater than $\sim$4$\mu$m, would be given by the dashed extrapolations of the 6000°K data in Figure 8. The high-intensity carbon-arc is a comparable source of radiation which can operate at a temperature of $\sim$6000°K in open air. Carbon arcs were in fact used, as a standard source for high intensity searchlights, long before the high pressure xenon-arc was developed.[54] If our searchlight employed a carbon-arc source with no cover, then the data in Figure 8 show that a NE$\Delta$T of of $\sim$0.1°K would permit S191 to detect the beam, in the thermal-infrared spectral interval from $\sim$7.5 to $\sim$8.5$\mu$m, at the orbital altitude of Skylab-A.

### 3.4 Discussion of the Final Results

The primary results of this exercise are summarized in Figure 8. Three fundamental conditions were imposed to simplify the formulation of the curves in this figure.

First of all, note that the curves of spectral radiant intensity ($J_\lambda$) in Figure 8 have not been multiplied by the atmospheric transmission function $\tau_\lambda$. The generality of the final results are not invalidated, however, because this correction is the same, at any specific viewing angle, for both the searchlight and any surface target. Note, however, that the noise-equivalent-spectral-radiance (i.e., NESR) is a sensitivity threshold which is dependent only on the properties of the spectrometer. The noise-equivalent-temperature-difference (i.e., NE$\Delta$T) is an artifice which is used to express this threshold in terms of a change in target temperature. Since the radiance data for NE$\Delta$T in Figure 8 are for perfect atmospheric transmission, it follows from Appendix D that if this transmission is reduced to $\tau_\lambda$, then a change in target temperature of NE$\Delta$T/$\tau_\lambda$ is required to produce a signal equal to the noise threshold of the spectrometer.

The second condition is that the area of the target is determined by what would fill the field-of-view of S191 in the nadir direction from the altitude of Skylab-A. Target areas defined in this way become larger for off-nadir viewing angles which do not include the horizon in the field-of-view. Nevertheless, as shown in Appendix B, the spectral power that would be received by S191 is independent of the viewing angle if the target surface is Lambertian. On the other hand, the spectral power received by S191 from the searchlight would be greater at nadir than when it is viewed off-nadir. The relative reduction in intensity would be equal to the square of the ratio of the searchlight-to-detector distance for these two situations.

The third condition is that S191 remain in the searchlight beam for one complete scan (i.e., $\sim$1 sec.). In fact, however, a key attribute of the proposal by Belz[1] is the relaxed restriction that the searchlight beam sweep over the spacecraft many times during overflight of the target. The duration of the flashing signal would be shortest when the spacecraft is directly over the center angle of the searchlight oscillation. As a specific example, consider a searchlight oscillation of $\pm 20°$ about the local vertical at a frequency of 1 cps. The skylab would move through this arc about the local vertical in about 44 sec. It would therefore be exposed to $\sim$88 flashes. For a full beamwidth of 2°, the flash duration directly over local vertical at the Skylab altitude would be about 8 millisec[1]. There would be two flashes during each of the 1-sec spectral scans by S191, and therefore the total illumination

time during each scan with the searchlight at nadir would be ∿16 millisec. At the end-points of the searchlight oscillation, the corresponding total illumination interval during each scan would be ∿0.1 sec. As noted in Appendix C, however, the full beamwidth is ∿2° only at wavelengths for which radiation from the relatively small xenon arc can pass through the quartz envelope. This envelope is the opaque source of radiation for wavelengths between ∿4 and ∿50μm, and its large size produces a full beam spread of ∿27° in this spectral region. The initial assumption of continuous illumination of the spectrometer by the searchlight is therefore not overly conservative for thermal-infrared radiation.

As stated in the introduction, a primary purpose of this report was to determine if thermal-infrared radiation (i.e., ∿8 to ∿13μm) from the Belz searchlight beacon would contaminate radiometric measurements by S191 of surface targets at night. The results presented here show that, in the thermal-infrared region, S191 would receive less spectral power (at the 435 km orbital altitude of Skylab-A), from a 20-kW xenon-arc searchlight, than from that produced by a ∿0.1°K change in the temperature of a typical surface target. Current specifications for S191 indicate that it would not detect variations in spectral power which are less than that caused by a ∿1°K change in target temperature.[5]

As noted in the introduction, this problem is somewhat academic. In fact, the searchlight could have been made acceptable as a target marker even if the calculations here had indicated that thermal-infrared radiation in the beam would be detectable by S191. The intensity of this radiation could be readily reduced to an acceptable level by passing the beam through a quartz plate, which is opaque in the thermal infrared region of the spectrum.[54] Nevertheless, this problem has provided a useful exercise for developing physical insight about some of the measurement capabilities of S191.

## 4.0 CONCLUSIONS

The data reviewed in this report show that the reststrahlen spectral signatures of surface rocks and minerals will be very difficult to identify uniquely in the thermal-infrared spectra measured by S191 in space. Diurnal variations in signal strength, from different types of targets, offer a potential but unproven way of enhancing the information-to-noise ratio in spectral measurements which are made at optimum times of day or night. Calculations in this report show that

the 20-kW xenon-arc searchlight (with which Belz[1] proposed to mark targets for night-time acquisition by the astronauts on Skylab-A), would not contaminate measurements of surface targets made by the spectrometer (S191) in the thermal-infrared spectral region.

It must be emphasized that only passive measurements, made in a very narrow region of the electromagnetic spectrum, were considered here. The ultimate capabilities of remote-sensing measurements made in space, for obtaining quantitative information about surface targets, will undoubtedly rest on the success of active as well as passive measurements made simultaneously over wide regions of the electromagnetic spectrum. Research from aircraft, and possibly from balloon platforms, should be intensified in order to develop techniques for improving the probability that space-based measurements of Earth-Resources targets will become increasingly successful and useful.

## 5.0 ACKNOWLEDGMENTS

The author would like to acknowledge several stimulating discussions with D. J. Belz, R. E. McGaughy, W. L. Smith, and A. R. Vernon. It is also a pleasure to acknowledge the full cooperation of the library, drafting, reproduction and stenographer staffs at Bellcomm.

1011-RWN-ajj

R. W. Newsome, Jr.

Attachments

## REFERENCES


1. Belz, D.J., "Optical Beacons for Acquisition and Tracking of S191 Targets During Night-Side Passes", Bellcomm Technical Memorandum TM-71-1025-2, April 22, 1971.

2. Newsome, R.W., Jr., "Transmission of Infrared Radiation Between the Surface of the Earth and Space", Bellcomm Technical Memorandum TM-71-1011-3, March 10, 1971.

3. Moller, F. and E. Raschke, "Problems of Meteorological Observations from Satellites", Space Science Reviews 9, 90, (1969).

4. Barnett, T.L., "Infrared Spectrometer, S-191, Experiment Implementation Plan", NASA Manned Spacecraft Center, November 13, 1969.

5. von Ehrenfried, M.H., Skylab-A EREP Users Handbook, March 1971, NASA-S-71-13209-F.

6. Hovis,W.A., W.A. Kley, and M. G. Strange, "Filter Wedge Spectrometer for Field Use", Applied Optics 6, No. 6, 1057, (1967).

7. Buettner, K.J.K. and C.D. Kern, "The Determination of Infrared Emissivities of Terrestrial Surfaces", J. Geophys. Res., 70, No. 6, 1329, (1965).

8. Goetz, A.F.H., "Differential Infrared Lunar Emission Spectroscopy," J. Geophys., Res. 73, 1455 (1968).

9. Bramson, M.A., Infrared Radiation: A Handbook for Applications, (Plenum Press, N.Y., 1968).

10. Young, J.B., H.A. Graham, and F.W. Peterson, "Wire Grid Infrared Polarizer", Applied Optics 4, No. 8, 1023, (1965).

11. LeGault, R., "Sources of Electromagnetic Radiation", AIAA Earth Resources Observations and Information Systems Meeting, Annapolis, Md./March 2-4, 1970 (AIAA Paper No. 70-287).

12. Garbuny, M., Optical Physics,(Academic Press, New York, 1965).

13. Lyon, R.J.P., "Evaluation of Infrared Spectrophotometry for Compositional Analysis of Lunar and Planetary Soils, Part 2: Rough and Powdered Surfaces", NASA Rept. CR-100, 1964.

14. Vickers, R.S. and R.J.P. Lyon, "Infrared Sensing from Spacecraft: A Geological Interpretation," in Thermophysics of Spacecraft and Planetary Bodies, Vol. 20, (ed., G.B. Heller), p. 585 (AIAA, 1967).

15. Jacobs, J.A., R.D. Russell, and J.T. Wilson, Physics and Geology, (McGraw-Hill Pub., New York, 1959).

16. Hovis, W.A., Jr., and W.R. Callahan, "Infrared Reflectance Spectra of Igneous Rocks, Tuffs, and Red Sandstone from 0.5 to 22μm", J. Opt. Soc. Am. 56, 639 (1966).

17. Spitzer, W.G., and D.A. Kleinman, "Infrared Bands of Quartz", Phys. Rev. 121, no. 5, 1324 (1961).

18. Aronson, J.R. and A.G. Emslie, "The Influence of Physical Variables on Spectral Signatures on Natural Targets", Arthur D. Little, Inc., (December 31, 1969), prepared for Air Force Cambridge Research Laboratories, AFCRL-70-0083, AD-702-532.

19. Conel, J.E., "Infrared Emissivities of Silicates: Experimental Results and a Cloudy Atmospheric Model of Spectral Emission from Condensed Particulate Mediums", J. Geophys. Res. 74, no. 6, p. 1614, (1969).

20. Šimon, I., and H.O. McMahon, "Study of the Structure of Quartz, Cristobalite, and Vitreous Silica by Reflection in Infrared", J. Chem. Phys. 21, No. 1, 23 (1953).

21. Hudson, R.D., Jr., Infrared System Engineering, (Wiley-Interscience, New York, 1969).

22. Pivovonsky, M., and M.R. Nagel, Tables of Blackbody Radiation Functions, (The MacMillan Co., New York, 1961).

23. Watson, K., L.C. Rowan, and T.W. Offield, "Application of Thermal Modeling in the Geologic Interpretation of IR Images", in Proceedings of the Seventh International Symposium on Remote Sensing of Environment, p. 2017, (Ann Arbor, Michigan/May 17-21, 1971).

24. Daly, R.A., Igneous Rocks and the Depths of the Earth, (McGraw Hill pub., New York, 1933).

25. Pettijohn, F.T., Sedimentary Rocks, (Harper & Brothers pub., New York, 1949).

26. "The University of Michigan Notes for a Program of Study in Remote Sensing of Earth Resources", Willow Run Laboratories, Contract NASA 9-7676, November, 1968.

27. Brennan, P.A. and J. Lintz, Jr., "Remote Sensing of Some Sedimentary Rocks", in Proceedings of the Seventh International Symposium on Remote Sensing of Environment, p. 253, (Ann Arbor, Michigan/May 17-21, 1971).

28. Holter, M.R. in Remote Sensing: With Special Reference to Agriculture and Forestry, (pp. 73-161 and 354-412), (compiled by the Committee on Remote Sensing for Agricultural Purposes, (J.R. Shay, Chairman); National Research Council, National Academy of Sciences; Washington, D.C., 1970)

29. Johnson, P.L. (editor), Remote Sensing in Ecology, (University of Georgia Press, Athens, 1969).

30. Anding, D., R. Kauth, and R. Turner, "Atmospheric Effects on Infrared Multispectral Sensing of Sea-Surface Temperature from Space", Willow Run Laboratories, The University of Michigan, NASA Report CR-1858 (July, 1971).

31. Wolfe, W., Handbook of Military Infrared Technology, Office of Naval Research; Department of the Navy; Washington, D.C. (1965).

32. Clark, H.L., "Some Problems Associated with Airborne Radiometry of the Sea", Applied Optics 6 no. 12, p. 2151 (1967).

33. Hovis, W.A., Jr., "Optimum Wavelength Intervals for Surface Temperature Radiometry", Applied Optics 5, no. 5, 815, (1966).

34. Wallace, R.E. and R.M. Mozham, "Use of Infrared Imagery in Study of the San Andreas Fault System", (U.S. Geological Survey, 1965), NASA STAR Index N70-41074.

35. Campbell, R.W., Jr., L.D. Hoover, and F. Quero-Suñe, "Detailed Ground Study of 8-13 Micron Infrared Imagery", (Stanford University, 1969), N70-33736.

36. Vincent, R.K. and F.J. Thomson, "Discrimination of Basic Silicate Rocks by Recognition Maps Processed from Aerial Infrared Data", in Proceedings of the Seventh International Symposium on Remote Sensing of Environment, (p. 247, Ann Arbor, Michigan, May 17-22, 1971).

37. van Dijk, C., C.J. Mulder, J. Ph. Poley, and J. van Steveninck, "Exploration for (Shallow) Geological Structures with the Thermal Infrared Imagery Technique is Some Desert Areas of Oman", in Proceedings of the Seventh International Symposium on Remote Sensing of Environment, (p. 2115, Ann Arbor, Michigan; May 17-22, 1971).

38. Shilin, B.V., N.A. Gusev, M.M. Miroshnikov, Ye. Ya. Karizhenski, "Infrared Aerial Survey of the Volcanoes of Kamchatka", in Proceedings of the Sixth International Symposium on Remote Sensing of Environment, (p. 175, Michigan; October 13-16, 1969).

39. Bandeen, W.R., "Experimental Approaches to Remote Atmospheric Probing in the Infrared from Satellites", NASA, TM-X-63188, (May 1968), N68-22924.

40. Rao, P.K., A.E. Strong, and R. Koffler, "Sea Surface Temperature Mapping Off the Eastern United States Using NASA's ITOS Satellite", in Proceedings of the Severth International Symposium on Remote Sensing of Environment, (p. 683, Ann Arbor, Michigan; May 17-21, 1971).

41. Hovis, W.A., Jr., L.R. Baline, and W.R. Callahan, "Infrared Aircraft Spectra Over Desert Terrain 8.5μ to 16μ", Applied Optics 7, no. 6, 1137, (1968).

42. Lyon, R.J.P. and J. Patterson, "Airborne Geological Mapping Using Infrared Emission Spectra", in Proceedings of the Sixth International Symposium on Remote Sensing of Environment. (p. 527, Ann Arbor, Michigan; October 13-16, 1969).

43. Conrath, B.J., R.A. Hanel, V.G. Kunde, and C. Prabhakara, "The Infrared Interferometer Experiment on Nimbus 3", J. Geophys. Res. 75, no. 30, 5831 (1970).

44. Hanel, R.A., B. Schlachman, F.D. Clark, C.H. Prokesh, J.B. Taylor, W.M. Wilson, and L. Chaney, "The Nimbus 3 Michelson Interferometer", Appl. Opt., 9, 1769 (1970).

45. Hanel, R.A., B. Schlachman, D. Rogers, and D. Vanous, "Nimbus 4 Michelson Interferometer", Applied Optics, 10, no. 6, 1376 (1971).

46. Lyon, R.J.P., "The Multiband Approach to Geological Mapping from Orbiting Satellites: Is it Redundant or Vital?", AIAA Earth Resources Observations and Information Systems Meeting, (Annapolis, Maryland/March 2-4, 1970, AIAA Paper No. 70-303).

47. Freeman, R. S. and R. J. Ayling, "Xenon Arc Searchlight Illumination of the Apollo 8 Launch Area", Journal of the Society of Motion Picture and Television Engineers, 79, no. 4, p. 313 (April, 1970).

48. Thouret, W. E., H. S. Strauss, S. F. Cortorillo, and H. Kee, "High-Brightness Xenon Lamps with Liquid-Cooled Electrodes", Illuminating Engineering, 66 p. 339 (1965).

49. Lienhard, O. E., "Xenon Compact-Arc Lamps with Liquid-Cooled Electrodes", Illuminating Engineering, 60, p. 348 (1965).

50. Nakamura, Y., "An Improved High-Power Xenon Short-Arc Lamp", J. of Spacecraft & Rockets, 7 no. 4, p. 484 (April, 1970).

51. Stewart, J. E., Infrared Spectroscopy, (Marcel Dekker, Inc., New York, 1970).

52. McCarthy, D. E., "The Reflection and Transmission of Infrared Materials: I, Spectra from 2-50 Microns", Appl. Opts. 2, no. 6, 591 (1963).

53. Klein, L., "Measurements of Spectral Emission and Absorption of a High Pressure Xenon Arc in the Stationary and the Flashed Modes", Applied Optics 7, no. 4, p. 677, (1968).

54. Taylor, J. H. and H. W. Yates, "Atmospheric Transmission in the Infrared", Naval Research Laboratory Report 4759, July 2, 1956, Washington, D. C. (AD 103543 Unclassified).

55. "Preliminary Design Review of the Skylab Viewfinder/ Tracking System", September 8-10, 1970; Martin Marietta Denver Division.

56. Kaufman, J. E. (editor), IES Lighting Handbook, (Illuminating Engineering Society, 1966).

57. McMahon, H. O., "Thermal Radiation from Partially Transparent Reflecting Bodies", J. Opt. Soc. Am. 40, no. 6, 376 (1950).

58. Morse, P. M., Thermal Physics, (W. A. Benjamin, Inc., New York, 1969).

59. Jamieson, J. A., R. H. McFee, G. N. Plass, R. H. Grube, and R. G. Richards, Infrared Physics and Engineering, (McGraw-Hill, 1963).

60. Hanel, R. A., "Recent Advances in Satellite Radiation Measurements", in Advances in Geophysics, Vol. 14, Precision Radiometry, (edited by A. J. Drummond, Academic Press, 1970).

61. Anderson, G. M. and R. J. Ravera, "S-192 Multispectral Scanner Review", Bellcomm Memorandum B71-06007 (June 4, 1971).

TABLE 1 - COMPARISONS OF SOME MEASUREMENT CAPABILITIES OF S191 ABOARD SKYLAB-A WITH THOSE OF SPECTROMETERS ALREADY FLOWN ON OTHER MISSIONS

| INSTRUMENT | MISSION | SPECTRAL RANGE IN THERMAL IR-REGION ($\mu$m) | WAVELENGTH RESOLUTION IN THIS SPECTRAL REGION ($\mu$m) | NOISE-EQUIVALENT-SPECTRAL-RADIANCE ($W/cm^2$-ster-$\mu$m) | ANGULAR RESOLUTION (FULL ANGLE IN RADIANS) | ALTITUDE OF MISSION (km) | DIAMETER OF INSTANTANEOUS GROUND-RESOLUTION ELEMENT (km) | TIME FOR COMPLETE SPECTRAL SCAN (sec) | LENGTH OF GROUND TRACK SWEPT OUT IN 1 SCAN (km) |
|---|---|---|---|---|---|---|---|---|---|
| FILTER-WEDGE SPECTROMETER (S191) | SKYLAB – A ~1974 (REFS. 4, 5) | 6.2 – 15.5 | ~0.1 | $\sim 10^{-5}$ | $10^{-3}$ (0.057°) | 435 | 0.435 (0.235 N. MI.) | 1 | $\lesssim$1.85 ($\lesssim$1 N. MI.) {ASTRONAUT USED FOR TRACKING} |
| FILTER-WEDGE SPECTROMETER | NASA CONVAIR – 990 1967 (REF. 41) | 8 – 16 | ~0.2 | (NOT AVAILABLE) | $3.48 \times 10^{-2}$ (2°) | 0.7 – 10 | 0.0244 – 0.348 (80 – 1140 FT) | 30 | ~4 (~2.17 N. MI.) |
| FILTER-WEDGE SPECTROMETER | NASA P3A (ELECTRA) 1967 – 1969 (REF. 42) | 6.7 – 13.4 | ~0.1 | (NOT AVAILABLE) | $7 \times 10^{-3}$ (0.4°) | 0.61 – 2.74 | (0.00426 – 0.019) (14 – 63 FT) | 1/6 | $\sim 1.55 \times 10^{-2}$ (~51 FT.) |
| MICHELSON INTERFEROMETER | NIMBUS – 3 1969 (REFS. 43, 44) | 5 – 25 | $\Delta\lambda$ \| $\lambda$<br>0.03 \| 8<br>0.05 \| 10<br>0.08 \| 13 | $\sim 10^{-5}$ | $1.39 \times 10^{-1}$ (8°) | ~1100 | ~153 (~83 N. MI.) | 10.9 | ~68 (~37 N. MI.) |
| MICHELSON INTERFEROMETER | NIMBUS – 4 1970 (REF. 45) | 6.25 – 25 | $\Delta\lambda$ \| $\lambda$<br>0.02 \| 8<br>0.03 \| 10<br>0.05 \| 13 | $\sim 10^{-5}$ | $8.71 \times 10^{-2}$ (5°) | ~1100 | ~96 (~52 N. MI.) | 13.1 | ~81.5 (~44 N. MI.) |

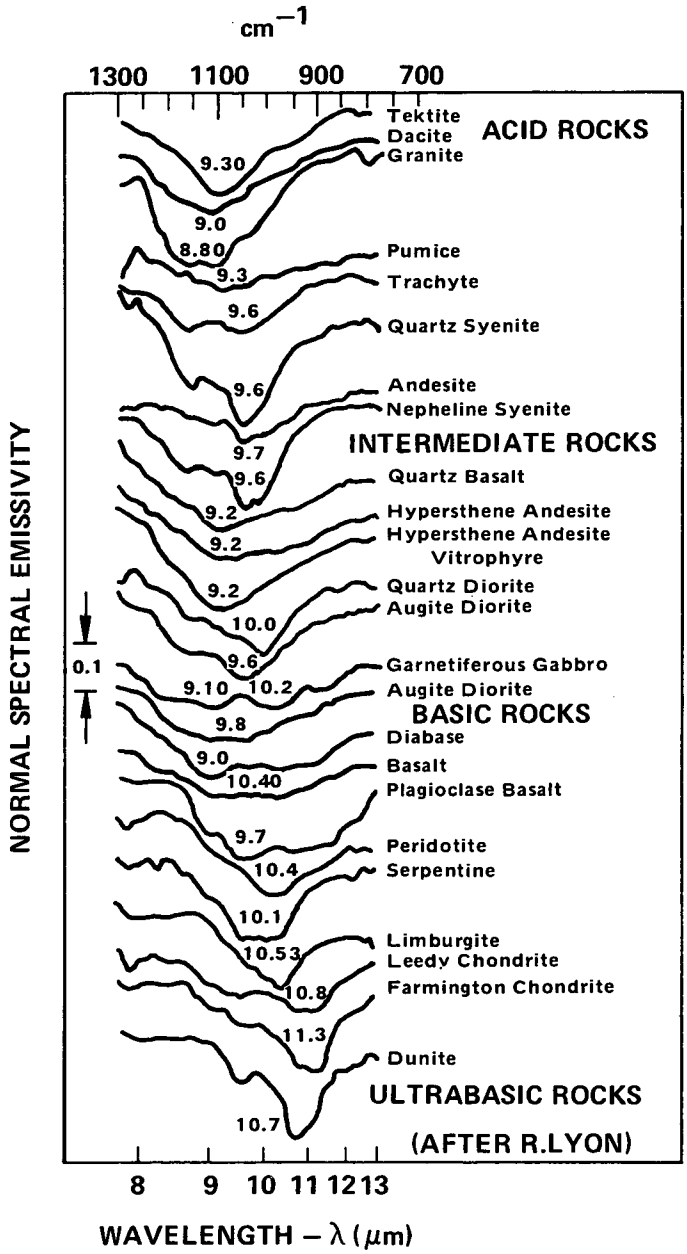


FIGURE 1 - RESTSTRAHLEN MINIMA IN THE EMISSION SPECTRA OF VARIOUS ROCK TYPES.[14]

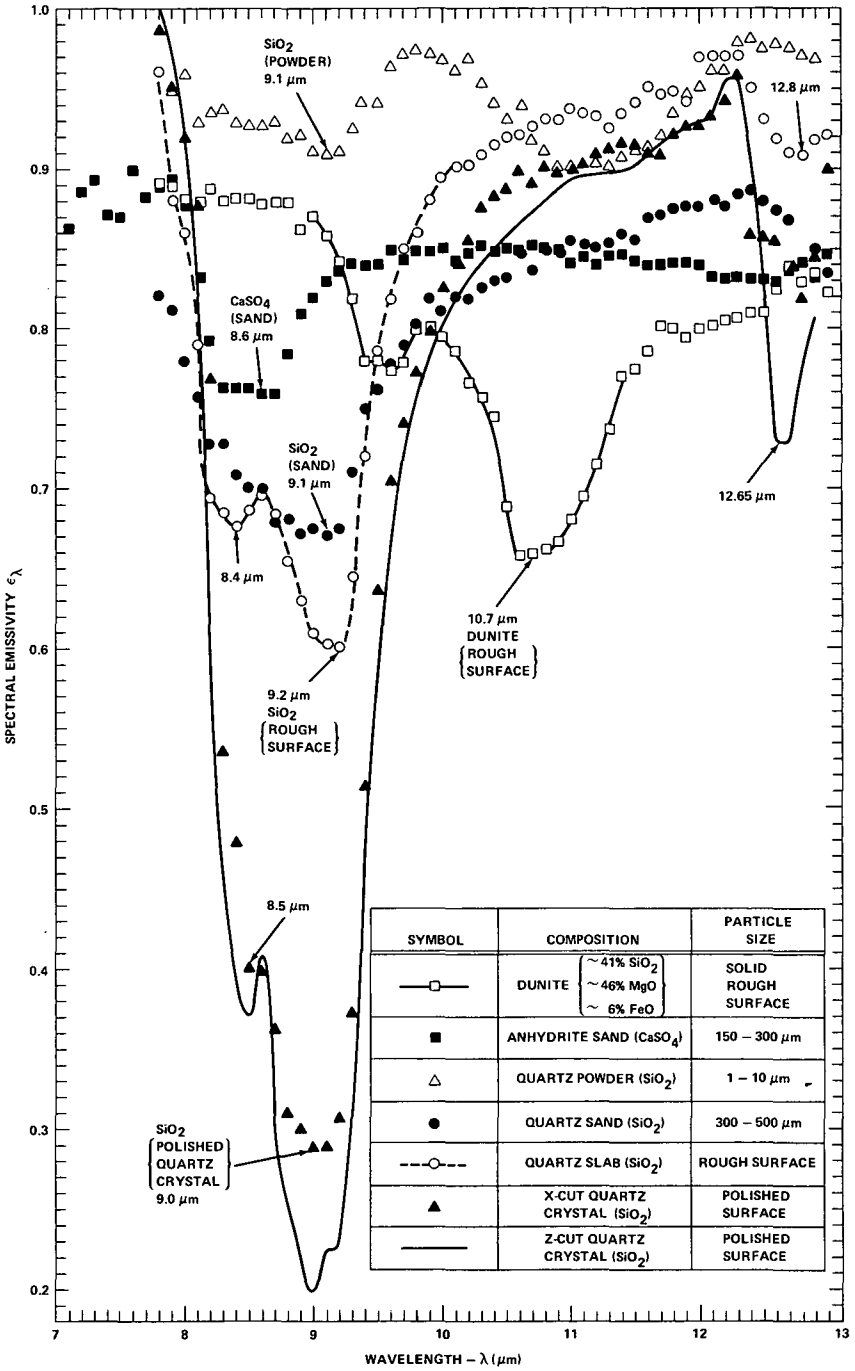


FIGURE 2 - A COMPOSITE SUMMARY OF SOME DATA OBTAINED FROM LABORATORY MEASUREMENTS OF THE SPECTRAL EMISSIVITY OF SEVERAL ROCKS AND SANDS[13]

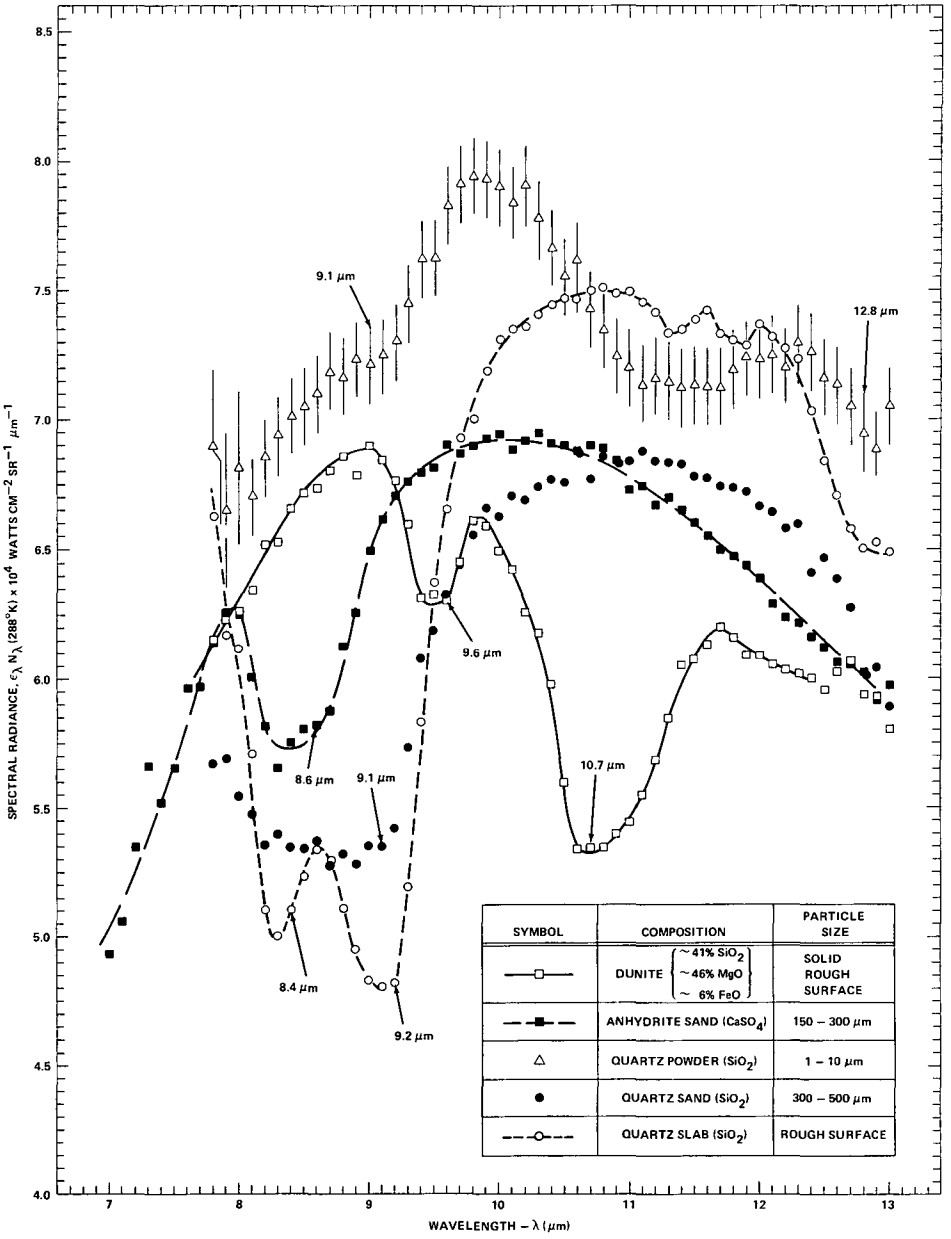


FIGURE 3 - PLOTS OF THE SPECTRAL INTENSITY OF THERMAL-INFRARED RADIATION EMITTED BY SEVERAL ROCKS AND SANDS AT THE AVERAGE TEMPERATURE OF THE SURFACE OF THE EARTH. THIS SPECTRAL RADIANCE IS THE PRODUCT OF THE SPECTRAL EMISSIVITY $\epsilon_\lambda$ WITH THE PLANCK RADIATION FUNCTION $N_\lambda(T)$ AT TEMPERATURE T = 288°K. THE VERTICAL ERROR BARS, ATTACHED TO THE SYMBOLS FOR QUARTZ POWDER, REPRESENT ± NESR (i.e., NOISE-EQUIVALENT-SPECTRAL-RADIANCE) FOR THE SPECTROMETER (S191)[5]

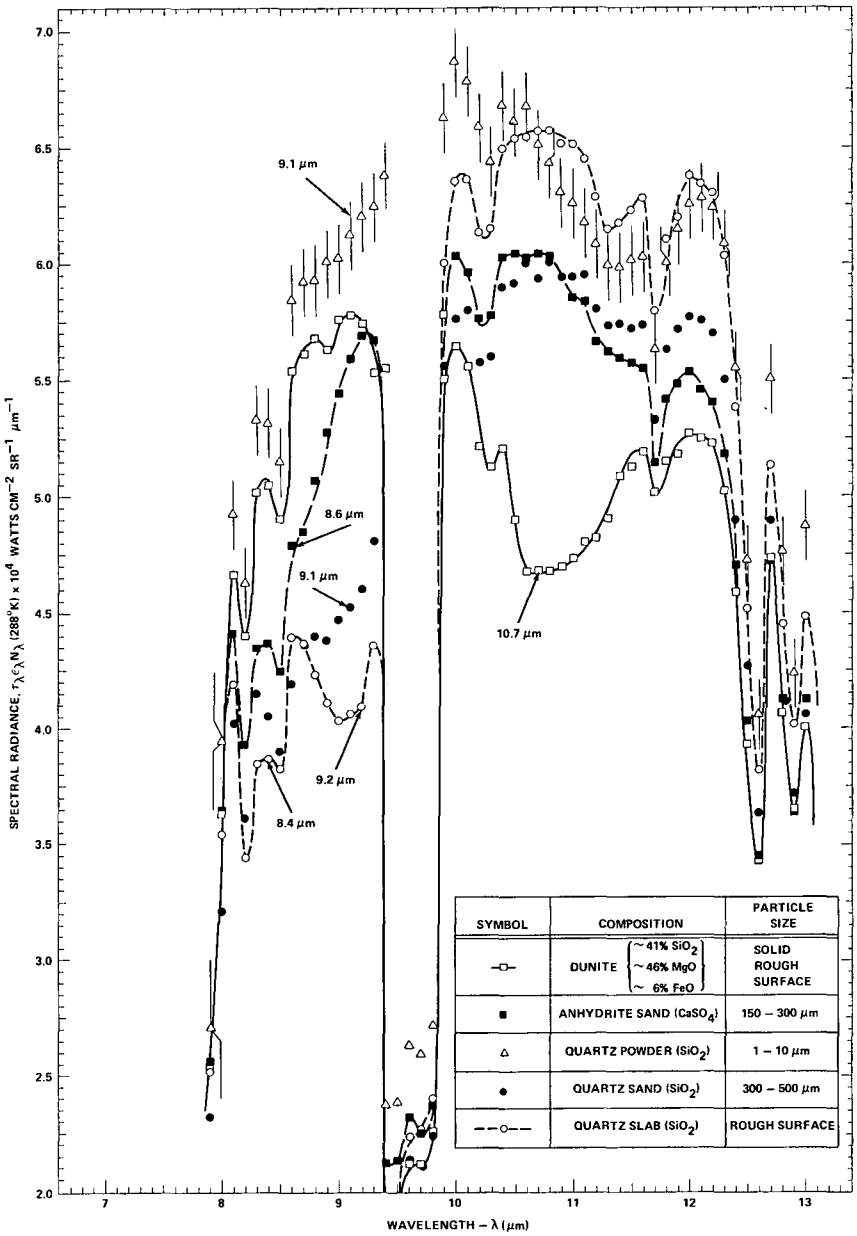


FIGURE 4 - INCLUSION OF ATMOSPHERIC TRANSMISSION EFFECTS TO ESTIMATE THE SPECTRAL RADIANCE IN SPACE DUE TO SPECIFIC ROCKS AND SANDS ON THE SURFACE OF THE EARTH AT A TEMPERATURE OF 288°K. THE SPECTRAL TRANSMISSION $\tau_\lambda$ FOR A VERTICAL PATH THROUGH THE ATMOSPHERE WAS OBTAINED FROM TABLES BY HUDSON[21] FOR EFFECTIVE SEA-LEVEL PATH LENGTHS OF 1.1 pr-cm OF WATER VAPOR, 4.1 km OF $CO_2$, AND 0.35 atm-cm OF OZONE.[2] THE VERTICAL ERROR BARS REPRESENT ± NESR FOR THE SPECTROMETER (S-191).[5]

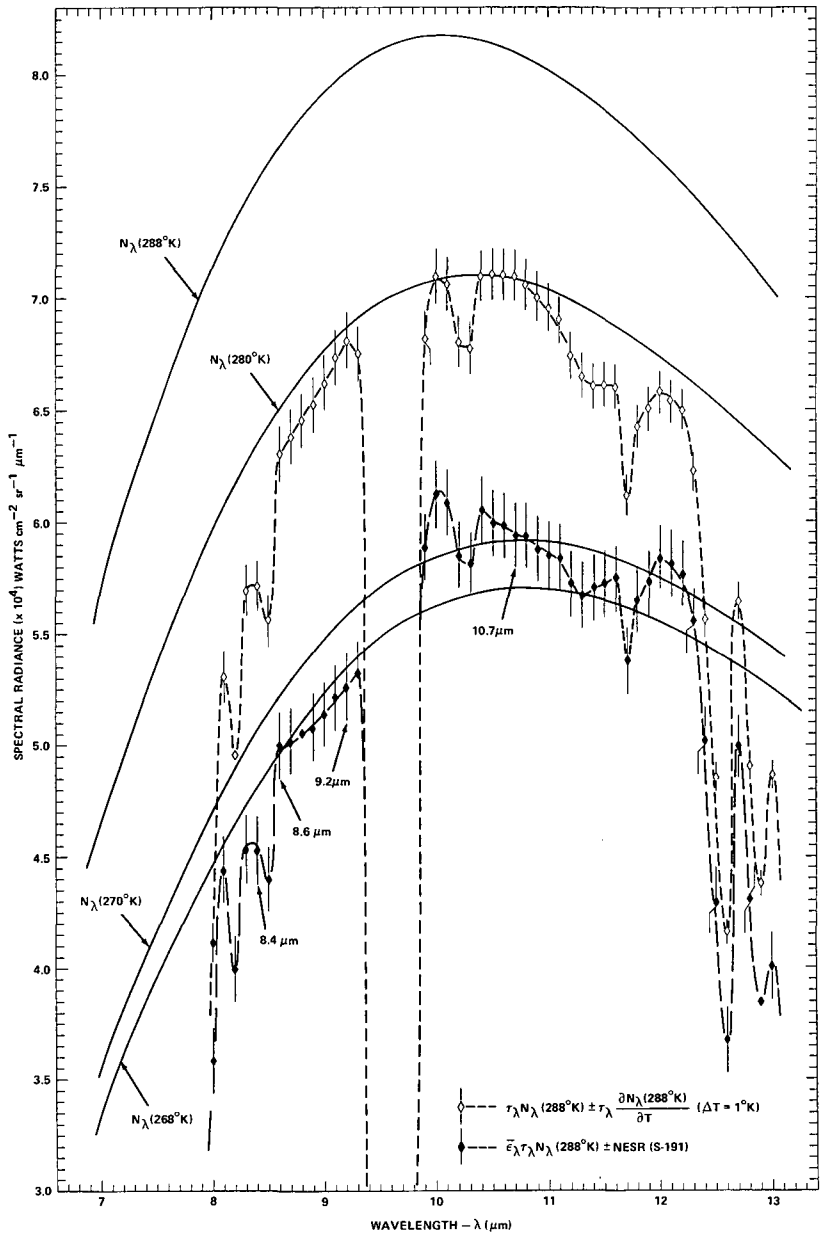


FIGURE 5 - COMPARISON OF THE SPECTRAL RADIANCE FROM A PERFECT RADIATOR (i.e., $\epsilon_\lambda = 1$) WITH THAT FROM A HOMOGENEOUS MIXTURE OF THE FIVE ROCKS AND SANDS FROM FIGURE 4, WHICH HAVE AN AVERAGE EMISSIVITY $\bar{\epsilon}_\lambda$. THE ABOVE FIGURE ALSO CONTAINS THE PLANCK RADIATION CURVES $N_\lambda(T)$ AT SEVERAL TEMPERATURES. THE SPECTRAL TRANSMISSION $\tau_\lambda$ FOR A VERTICAL PATH THROUGH THE ATMOSPHERE WAS CALCULATED FOR THE CONCENTRATIONS OF GASEOUS ABSORBERS LISTED IN THE CAPTION UNDER FIGURE 4

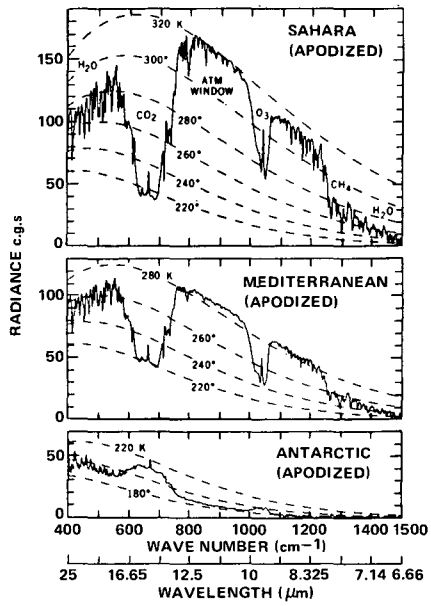


FIGURE 6a - REDUCED DATA, FROM REF. 45, OF THE THERMAL EMISSION SPECTRA RECORDED BY THE MICHELSON INTERFEROMETER IRIS-D ON NIMBUS 4. THE SPECTRA TAKEN OVER THE SAHARA DESERT SHOW AN EFFECTIVE TEMPERATURE, IN THE ATMOSPHERIC TRANSMISSION WINDOW FROM ~8.3 TO ~9.3 μm, WHICH IS ~10°K LOWER THAN IN THE WINDOW FROM ~10 TO ~12.5 μm. THIS IS THE ONLY DISCERNABLE INDICATION OF RESTSTRAHLEN EFFECTS DUE TO THE DESERT SAND ($SiO_2$), AND IT IS IN GENERAL AGREEMENT WITH THE RESULTS SHOWN IN FIGURES 4 AND 5. NOTE THAT THE SPECTRA TAKEN OVER THE ANTARCTIC SHOW MORE ATMOSPHERIC LINES IN EMISSION THAN ABSORPTION, BECAUSE THE SURFACE IS COOLER THAN THE ATMOSPHERE. (A SMOOTHING OR APODISATION FUNCTION WAS APPLIED TO THE ORIGINAL INTERFEROGRAMS IN ORDER TO REDUCE THE SIDE LOBES OF THE INSTRUMENT FUNCTION.)

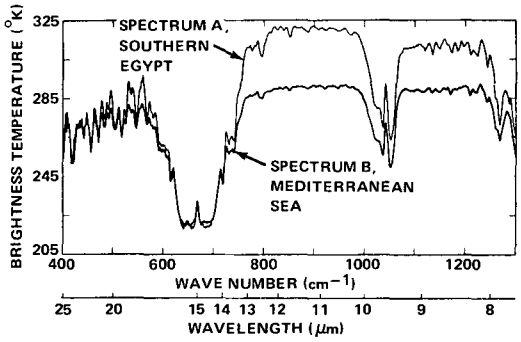


FIGURE 6b - REDUCED DATA, FROM REF. 43, OF THE THERMAL EMISSION SPECTRA RECORDED BY THE MICHELSON INTERFEROMETER IRIS-B ON NIMBUS 3. THESE SPECTRA HAVE BEEN PLOTTED IN TERMS OF THE EFFECTIVE BRIGHTNESS TEMPERATURE WHICH CORRESPOND TO THE RADIANCE MEASURED BY THE SPECTROMETER. AS IN THE FIGURE ABOVE, THE EFFECTIVE TEMPERATURE OVER SOUTHERN EGYPT IS LOWER IN THAT PARTICULAR ATMOSPHERIC WINDOW WHERE ONE WOULD EXPECT RESTSTRAHLEN DEPRESSIONS IN SURFACE EMISSIVITY DUE TO DESERT SAND (i.e., $SiO_2$). THIS EFFECT IS NOT OBSERVED IN THE SPECTRA TAKEN OVER THE MEDITERRANEAN SEA.

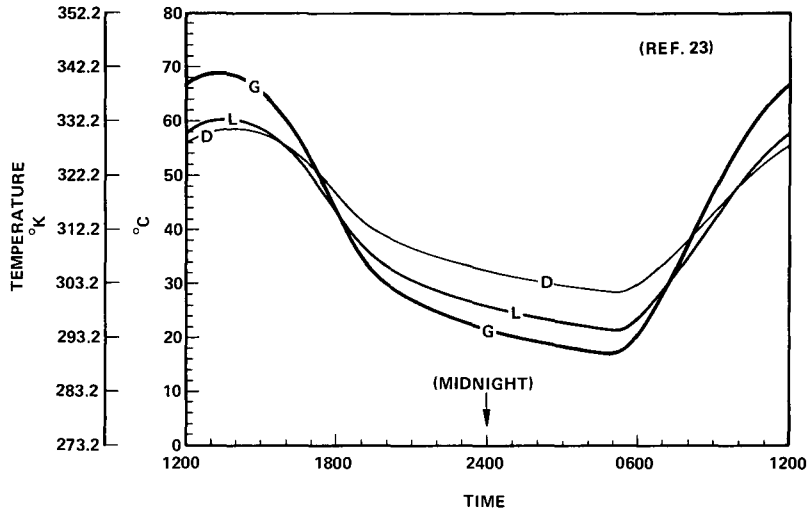


FIGURE 7a - PREDICTIONS OF DIURNAL VARIATIONS IN THE SURFACE TEMPERATURES OF LIMESTONE (L), DOLOMITE (D), AND GRANITE (G) IN MIDSUMMER. THE CALCULATIONS WERE BASED ON REPRESENTATIVE VALUES OF THE ALBEDO AND THERMAL INERTIAL OF THESE MATERIALS AT THE MILL CREEK, OKLAHOMA TEST AREA.[23]

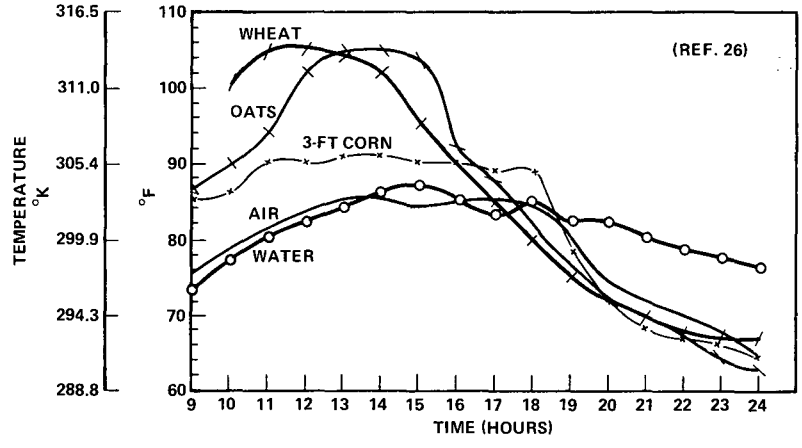


FIGURE 7b - TEMPERATURE VARIATIONS OF CROPS.[26]

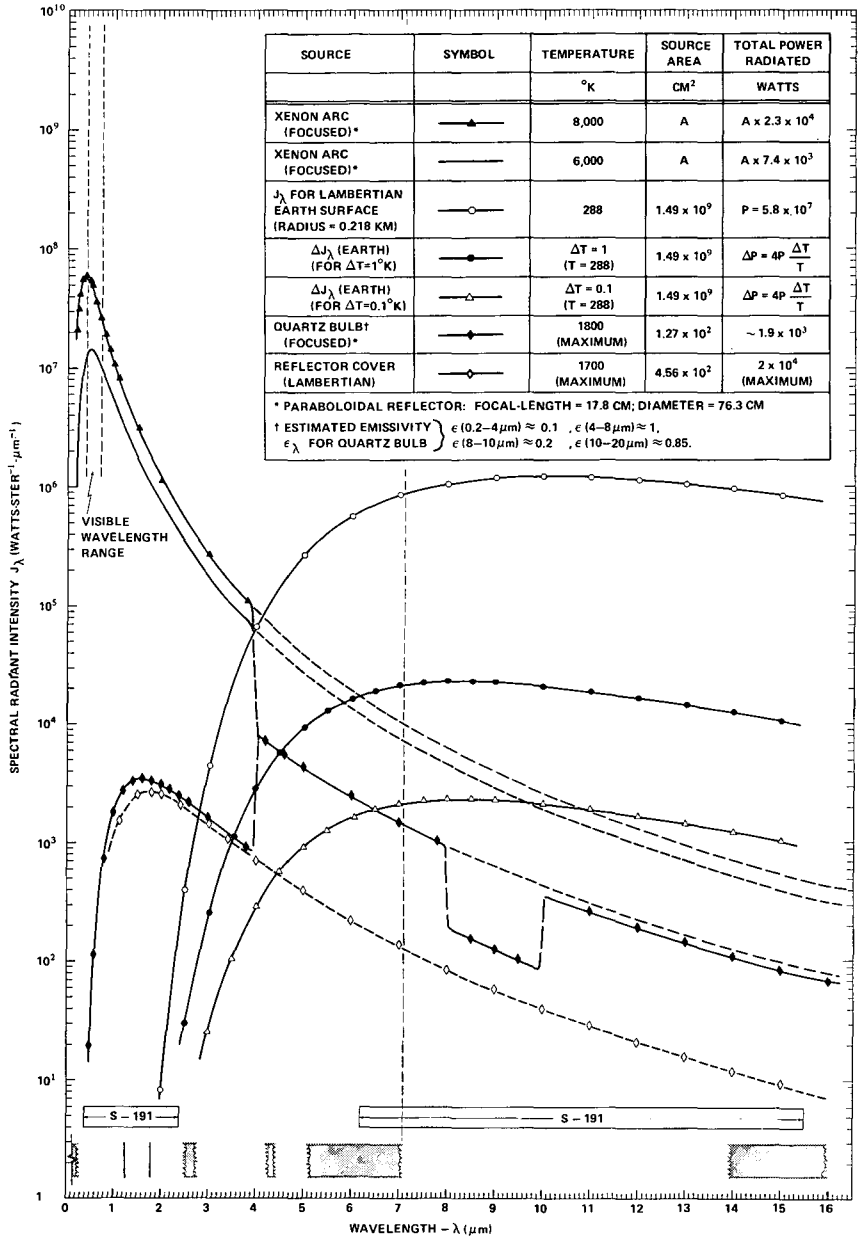


FIGURE 8 - COMPARISON OF THE ESTIMATED SPECTRAL RADIANT INTENSITY $J_\lambda$ (WATTS-STER$^{-1}$-$\mu m^{-1}$) FROM A S-191 SURFACE TARGET AT NIGHT, WITH THAT FROM A 20-kW XENON SEARCH LIGHT. THE AREA OF THE SURFACE TARGET IS DETERMINED BY THE FIELD-OF-VIEW OF S-191 FROM 435 kM, FOR A NADIR VIEWING ANGLE. THE PLOTTED SEARCH LIGHT INTENSITIES ARE FOR CONTINUOUS ILLUMINATION OF S-191. ALSO SHOWN ARE CURVES OF THE INCREMENTAL CHANGES IN $J_\lambda$ (EARTH) PRODUCED BY SURFACE TEMPERATURE VARIATIONS OF 1 AND 0.1°K. THE OPEN BARS SHOW THE SPECTRAL RANGES OF SENSITIVITY FOR S-191. THE SHADED BARS INDICATE THE WAVELENGTH INTERVALS FOR WHICH THE ATMOSPHERIC ATTENUATION ALONG A VERTICAL PATH BETWEEN EARTH AND SPACE IS $\geq$ 20 dB IN CLEAR WEATHER.

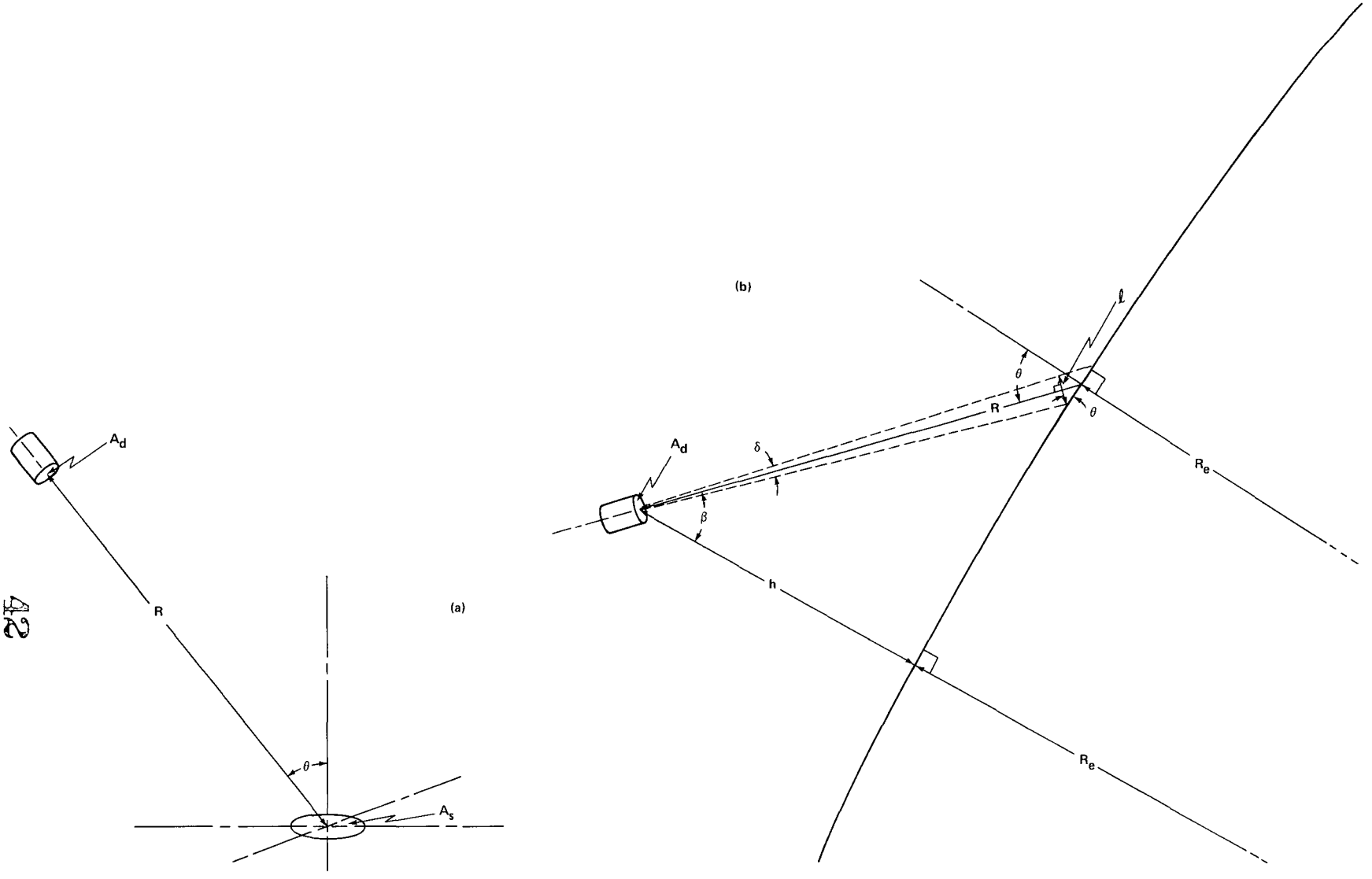


FIGURE 9 - PART (a) IS A DIAGRAM WHICH DEFINES THE PARAMETERS USED IN THE SMALL-ANGLE APPROXIMATION. PART (b) DEFINES THE CORRESPONDING PARAMETERS USED TO CALCULATE THE POWER RECEIVED BY AN ORBITING DETECTOR, WITH A FIXED ANGULAR FIELD-OF-VIEW ($\delta$), FROM A SURFACE TARGET WHICH IS VIEWED AT AN ANGLE ($\beta$).

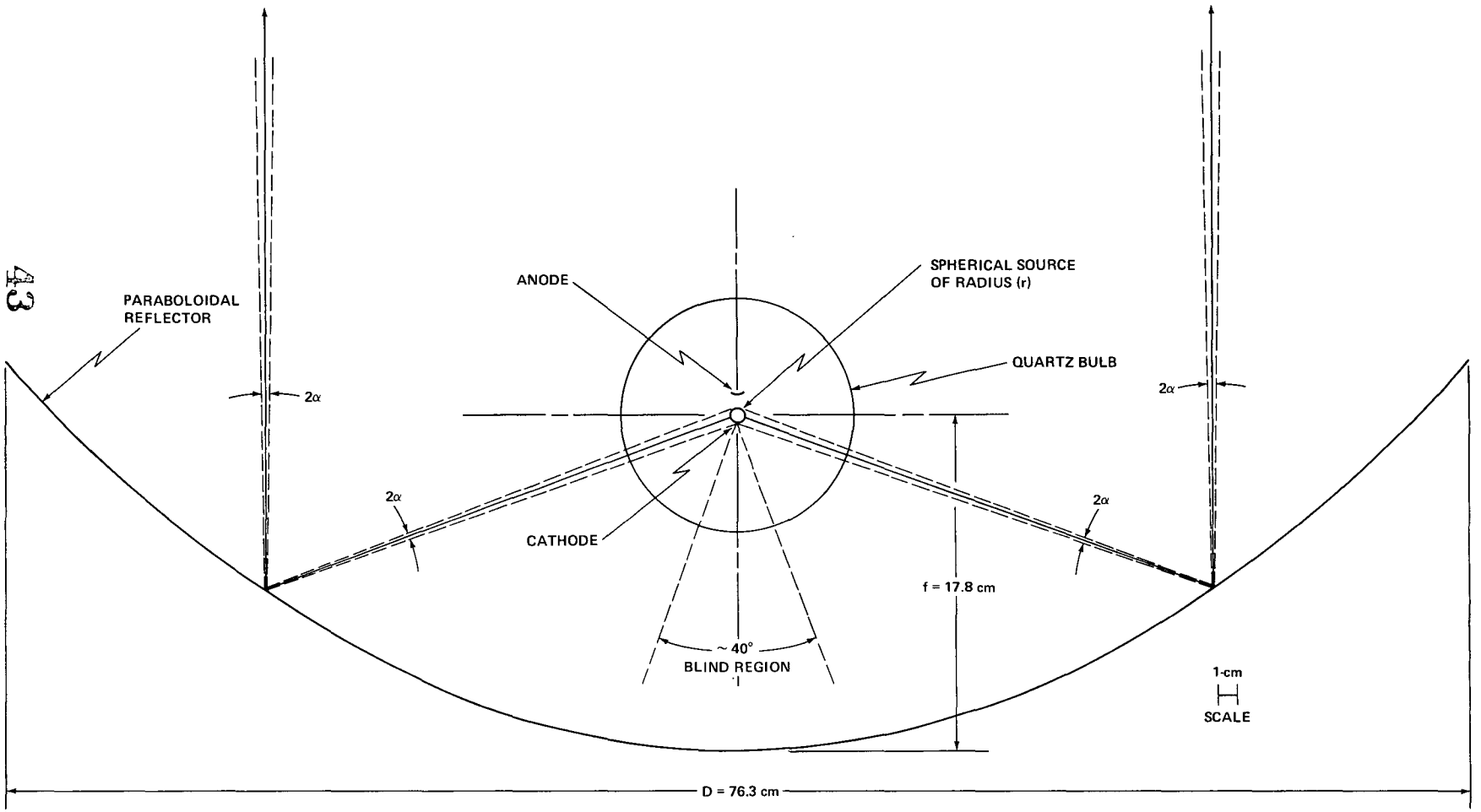


FIGURE 10 - THIS IS A SCALE DRAWING OF THE PARABOLOIDAL REFLECTOR WHICH FOCUSES THE 20-kW XENON SHORT-ARC LAMPS EMPLOYED AT THE APOLLO LAUNCH SITES. THE QUARTZ EXTENSION ARMS, WHICH HOUSE THE POWER LEADS AND WATER-COOLING CONNECTIONS, ARE NOT SHOWN. THE SPHERICAL AREA CORRESPONDING TO THE SOURCE RADIUS IN THIS SCHEMATIC IS EQUAL TO THAT REQUIRED TO RADIATE 20-kW FROM A PERFECT BLACKBODY AT 6000° K.

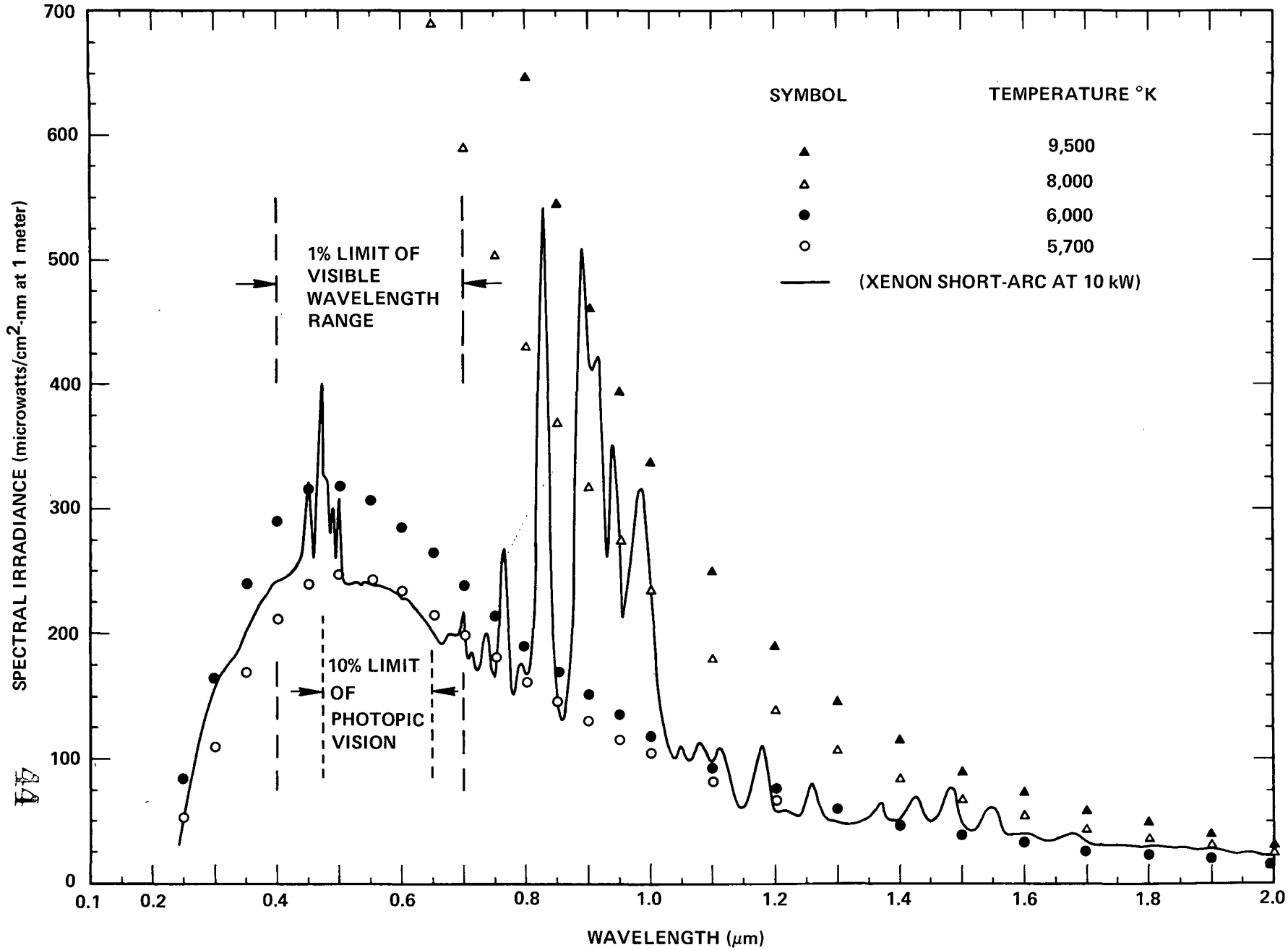


FIGURE 11 - THE SPECTRAL ENERGY DISTRIBUTION FROM A 10-kW SHORT-ARC XENON LAMP.[48] PLANCK BLACKBODY SPECTRA AT SEVERAL REPRESENTATIVE TEMPERATURES ARE ALSO INCLUDED

# APPENDIX A

## A GENERAL DESCRIPTION OF THE SPECTROMETER SUB-SYSTEMS

A Cassegrain optical system is located at the front of the spectrometer to collect and focus the incident radiation.[4,5,55] The focal length of the collection telescope is 63.5 cm, and the diameter of the primary mirror is 25.4 cm. A flat, gimbaled mirror is located in front of the primary mirror to permit off-nadir tracking 10° aft to 45° forward and ±20° across track. The field-of-view of the spectrometer is fixed at one milliradian. For nadir observations from the Skylab altitude of 435 km (i.e., 235 n.mi.), the diameter of a resolution element on the surface is 0.435 km.

An auxiliary viewfinder/tracking system permits an astronaut to use the visual spectral region to select and photograph targets. A pickoff mirror is located between the tracking mirror and the primary collection mirror. This arrangement permits the viewfinder telescope and camera to be boresighted with the Cassegrain optical system of the spectrometer. The preliminary design specifications for the viewfinder telescope call for a maximum field-of-view of 17° ± 1° at minimum magnification of 2.24 ± 10%.[55] Maximum magnification is not to exceed 10 times minimum magnification. The ground resolution at maximum magnification is to be 45.8 m(i.e., 150 ft.) for nadir viewing from an altitude of 435 km.[55]

Radiation from the Cassegrain optical system enters a beam splitter which separates the relatively long wavelength (i.e., thermal infrared) radiation from that in the visible and near infrared spectral region. The advantage of this separation is that subsequent stages of the detection systems could be designed for maximum sensitivity in each spectral region. The two beams are chopped at the beam splitter by an optical deflection system which inserts calibration sources into the field-of-view. These reference sources are kept at carefully controlled temperatures and they are viewed at regular intervals to provide continuous calibration of everything but the entrance optics of the spectrometer. Each of the two beams is then focused on a small area of a filter wheel, and the intensity of transmitted radiation is measured as a function of wavelength as the wheel is rotated. These filter wheels are essentially interference films which have been deposited with precise azimuthal variations in thickness.[6] An advantage of placing the chopper in front of the filter wheels is that the transmitted radiation is frequency modulated and can therefore be efficiently filtered from the steady background of infrared radiation emitted by the instrument. The two filter wheels in S191 cover the spectral intervals 0.4 to 2.4 μm and 6.2 to 15.5 μm, with spectral resolution of 1 to 2% in wavelength.[4,5] Note that the multispectral scanner (S192) has only one broad spectral channel (i.e., from 10.2 to 12.5 μm) in the thermal-infrared region.[5] By comparison,

this single channel is resolved into ∿11 wavelength intervals by the spectrometer (S191).

The radiation transmitted through each of the filter wheels is focused on a solid-state detector. The amplitude of the output signal is approximately proportional to the instantaneous power carried by the transmitted beam to the sensitive area of the detector. The NASA Experiment Implementation Plan recommended that the transmitted beam of thermal-infrared radiation (i.e., 6.2 to 15.5 μm) be monitored by a HgCdTe detector, cooled to 77°K.[4] Several detectors (e.g., Si, GaAs, PbSe, InAs or PbS) were considered to be acceptable for use in the wavelength intervals from 0.4 to 2.4 μm.[4]

The performance specification for the noise-equivalent-temperature-difference (NEΔT), which characterizes the sensitivity of the overall spectrometer/detector system in the spectral interval from 6.2 to 15.5 μm, was originally estimated to be NEΔT ∿ ± 0.1°K (with target and background at 300°K and no atmospheric considerations).[4] Currently, however, the EREP Users' Handbook shows that the average noise-equivalent-spectral radiance (NESR) for S191, over the atmospheric transmission window from 8 to 13 μm, is $1.5 \times 10^{-5}$ Watts/cm$^2$-ster-μm.[5] This is equivalent to a NEΔT of ∿1°K at a wavelength of ∿10 μm for a detector-noise-limited system which views a target, with unit emissivity at ∿288°K, through an atmosphere with perfect transmission.

The sensitivity of the spectrometer in the shorter wavelength interval (i.e., 0.4 to 2.4 μm) is expressed in terms of noise-equivalent-reflectance-difference (NE$\Delta\rho$), because the intensity of solar radiation at the surface of the Earth is much larger than thermal emission from the Earth in this spectral region. The value quoted in the Experiment Implementation Plan is NE$\Delta\rho \simeq \pm$ 1% (for solar radiance at Earth, and no atmospheric considerations).[4] The physical significance of NE$\Delta$T, NESR, and NE$\Delta\rho$, and their dependence on the spectrometer parameters and atmospheric transmission, are discussed in Appendix D.

An electronic system amplifies the electrical signals from the detectors and catalogs them on magnetic tape as a function of wavelength. The spectral labels are obtained from marker pulses which identify the orientation of each filter wheel as a function of time. This information is then correlated in time with the output signals from the detectors which monitor the intensity of radiation transmitted through the wheels.

APPENDIX B

## SOME FUNDAMENTALS OF RADIOMETRY IN THE SMALL ANGLE APPROXIMATION

In this appendix, some fundamentals of thermal radiometry in the small-angle approximation are summarized. This information is then used to calculate the total spectral power received by an instrument, with a small, fixed field-of-view. It is shown that this power is independent of the viewing angle, if the radiation is from a Lambertian surface which always fills the field-of-view of the detector, and if differences in atmospheric transmission are neglected.

Let us first consider the simplified problem, depicted in Figure 9a, of calculating the power received by the detector area ($A_d$) from a Lambertian radiator with surface area ($A_s$). We also assume that the target area ($A_s$) is at an equilibrium temperature (T), and that it completely fills the field-of-view of the detector. In the small-angle approximation, the distance (R) between the detector and target is great enough so that the finite-size of the detector and target areas can be neglected in the calculation of the solid angles which they subtend with respect to each other. In this approximation, we can immediately write down the spectral radiant intensity from the target:

$$J_\lambda(\Theta) = A_s \, \varepsilon_\lambda \, N_\lambda(T) \cos\Theta \quad \text{Watts-ster}^{-1}\text{-}\mu\text{m}^{-1} \quad , \qquad \text{(B-1)}$$

where $\varepsilon_\lambda$ is the spectral emissivity, and $N_\lambda(T)$ is the Planck blackbody function in Watts-cm$^{-2}$-ster$^{-1}$-$\mu$m$^{-1}$. The ($\cos\theta$) factor represents the well-known angular dependence of the intensity of radiation emitted from a Lambertian surface.(31) The total spectral power received by the detector area ($A_d$), oriented perpendicular to the line-of-sight, is:

$$P_\lambda(\theta) = \tau_\lambda(\theta)\ \Omega_d\ J_\lambda(\theta) \qquad \text{Watts-}\mu\text{m}^{-1}, \tag{B-2}$$

where $\tau_\lambda(\theta)$ is the spectral transmission function along the atmospheric path, and $\Omega_d$ is the solid angle subtended by the detector at the target. In the small angle approximation,

$$\Omega_d \cong A_d/R^2 \quad \text{ster}, \tag{B-3}$$

Combining the results of Equation B-1 through B-3, we obtain:

$$P_\lambda(\theta) = \varepsilon_\lambda\ \tau_\lambda(\theta)\ \frac{A_d\ A_s\ \cos\theta}{R^2}\ N_\lambda(T) \qquad \text{Watts-}\mu\text{m}^{-1}. \tag{B-4}$$

Note that the factor ($A_s\cos\theta/R^2$) is the solid angle ($\Omega_s$) which the target subtends at the detector.

Let us now consider the situation depicted in Figure 9b, of a detector in orbit above the Earth at an altitude (h). For nadir viewing, the target area in the fixed angular field-of-view ($\delta$) is:

$$A_s \cong \pi\left(\frac{h\delta}{2}\right)^2 \qquad \text{cm}^2. \tag{B-5}$$

The total power received by the detector can be obtained by inserting this result into Equation B-4 with $\theta = 0°$:

$$P_\lambda(0) = \varepsilon_\lambda \, \tau_\lambda(0) \, \frac{A_d \pi (h\delta)^2}{4 \, h^2} \, N_\lambda(T) \quad \text{Watts-}\mu\text{m}^{-1}. \tag{B-6}$$

Now let us consider the observation of a target at an angle ($\beta$) from nadir as in Figure 9b. The expression for the total power received by the detector will be the same as that in Equation B-4. The surface area ($A_s$) can be expressed in terms of the local vertical angle ($\theta$):

$$A_s(\theta) \cong \pi (R\delta)^2 / 4 \cos\theta, \tag{B-7}$$

where (R) is the detector-to-target distance. Insertion of this expression into Equation B-4 will cancel the factor $(\cos(\theta)/R^2)$. It follows that the ratio of the power received by the detector for nadir viewing, to that received at a viewing-angle $\beta$, is equal to:

$$P_\lambda(0)/P_\lambda(\beta) = \tau_\lambda(0)/\tau_\lambda(\beta), \tag{B-8}$$

where the same target temperature emissivity was assumed for both surface locations. If path differences in atmospheric transmission ($\tau_\lambda$) can be neglected, then the power flux received at the detector, (from Lambertian targets with the same emissivity and temperature), will in fact be the same for all viewing angles that do not include the horizon.

## APPENDIX C

## PERFORMANCE CHARACTERISTICS OF THE 20-kW XENON SEARCHLIGHT

This Appendix is a supplement to Section 3.2. It contains more detailed information about the published searchlight data, and about the procedures used to estimate additional performance characteristics.

### C.1 Published Information

The schematic drawing in Figure 10 represents the xenon-arc AN-TVS-3 searchlight set which Belz suggested for use as a target beacon.[1] It is in current use at the Apollo launch site at Cape Kennedy.[47] The radiation source for this searchlight is located at the focus of a paraboloidal reflector. As shown in Figure 10, this reflector has a focal length of 17.8 cm and a diameter of 76.3 cm.[47] It is made of electroformed nickel with a rhodium surface[47] which has a reflectivity of ∿96% in the wavelength region of ∿10μm.[21]

The light source is a 20-kW xenon short-arc lamp with liquid cooled electrodes. It was developed by the Duro-Test Corp. of North Bergen, N. J. The xenon is contained in a quartz tube which is 61 cm. in length and has a spherical shaped center which is 12.7 cm in diameter. The wall thickness of the quartz tube is ∿5mm,[48,49] and the pressure of the xenon gas during operation is approximately 9 atmospheres.[47]

The steady state electrical power load of this xenon lamp is 20-kW, at a nominal current of 465 amps at 43 volts dc. The xenon-arc in this lamp radiates approximately 50% of the this total input of electrical power.[49,50] The remaining power is partly dissipated at the anode and cathode terminals in amounts of ∿33% and ∿4% respectively, and ∿13% of the input power is lost by other mechanisms such as gas convection, etc.[49,50]

At a power level of 20-kW, the searchlight is capable of projecting a minimum peak candle power (i.e., lumens per steradian) of $8 \times 10^8$ with a focused beam width of ∿1.5°.[47] The limiting beam specification used by Belz[1] corresponds to a peak intensity of $\sim 8 \times 10^8$ candlepower, with a minimum luminous intensity of $\sim 8 \times 10^7$ candlepower within a divergence angle of $\pm$ 1°.

The 20-kW lamp used in the AN/TVS-3 searchlight has a reported color temperature of approximately 5500°K.[47] It must be assumed that only the visible part of the emission spectra was used to deduce this effective blackbody temperature. In general, there is relatively little spectral data about this type of searchlight in the published literature. Fortunately, an irradiance curve was located with spectral data out to 2μm from a similar xenon lamp.[48] This lamp operates at a power level of only 10-kW (i.e., 250 amps at 40 volts dc), with an internal pressure of ∿10 atmospheres. It has an arc gap of

9mm, as compared to the 14mm for the 20-kW lamp in Figure 10. In spite of these differences, the voltage gradient and the peak arc brightness for the two lamps are similar (i.e., 8000 candles/mm$^2$ and 6875 candles/mm$^2$ for the 10-kW and 20-kW lamps respectively), and therefore their emission spectra should be at least qualititively similar. This hypothesis is more than verified by the comparison in Figure 11 of spectral data from the 10-kW lamp with Planck radiation curves at several judiciously chosen temperatures. Note that a blackbody temperature of ∿5700°K gives a very good fit to the emission data over the spectral region corresponding to daylight (i.e., photopic) vision.[56] This is reasonably close to the reported color temperature of 5500°K for the 20-kW lamp.[47]

In Figure 11 the pressure-broadened spectral lines in the vicinity of ∿0.9μm deivate significantly from the Planck radiation curves corresponding to an equilibrium temperature of ∿6000°K. Similar spectral deviations might exist in the thermal-infrared region in the vicinity of 10μm. Fortunately, this possibility can be ignored for this problem because the quartz envelope is opaque to infrared radiation between the wavelengths of ∿4 and ∿50μm.[51,52] The heated quartz is therefore the primary source of thermal-infrared radiation for the searchlight. We will assume that any line-structure, due to radiative transitions in the quartz, will be severely broadened (i.e., with no spectral deviations in intensity which are

significantly larger than that predicted by the Planck function), as long as the quartz remains solid.

C.2 Deduction of the Thermal-Infrared Spectral Irradiance from the Xenon Lamp

As indicated in Figure 11, there is no single equivalent blackbody temperature which can be used to characterize all aspects of the spectrum from a high-pressure xenon-arc.[53] For the spectral regions of interest in this report, however, the effective average temperature of the entire arc will be assumed to be ∿6000°K.

A pragmatic check on the upper limit of the effective blackbody temperature, corresponding to the brightest part of the arc in the visible region, may be obtained as follows. The peak brightness of the cathode hot-spot for the 20-kW lamp is reported to be 6875 candles/mm$^2$. The equivalent blackbody temperature (T) which would produce this brightness can be obtained by solving the following integral equation:

$$685 \int_{0.41}^{0.70\mu m} Q_\lambda N_\lambda(T)\, \delta\lambda = 6{,}875 \text{ lumen-ster}^{-1}\text{-mm}^{-2} , \qquad \text{(C-1)}$$

where 685 lumens equal one watt at $\lambda$=0.555μm; $Q_\lambda$ is the daylight (i.e., photopic) efficiency of the eye, normalized to unity at $\lambda$=0.555μm;[56] $N_\lambda(T)$ is the Planck blackbody function in units of Watts-mm$^{-2}$-ster$^{-1}$-μm$^{-1}$; and one candle is defined as one lumen-ster$^{-1}$. An iterative trial and error approach was used to solve this equation for the temperature (T). Spectral

tables of $N_\lambda(T)$,[22] and $Q_\lambda$[56] were used to perform the integration in steps of $\delta\lambda$=0.01μm. Only three iterations were needed to obtain the temperature of the hot spot as T = 8,070°K.

As noted earlier, the quartz envelope is the effective source of thermal-infrared radiation in the searchlight beam. The temperature of the quartz must therefore be calculated in order to estimate the strength of this source of radiation. Quartz has a transmission window which extends from ∿0.2 to ∿4μm.[21] Transmission data and formulae in Reference 21 were then used to calculate the per-cent tranmission (including losses due to reflection and absorption) for a 5mm thick slab of quartz. It was found to be 93%, and this result was rounded-off to 90% in the following calculations. Quantitative information on the spectral emissivity of quartz is generally not available in the open literature,[21] and therefore the following procedure was used to estimate this data. The total spectral absorptance ($\alpha_\lambda$) reflectance ($\rho_\lambda$), and transmittance ($\tau_\lambda$) of any medium are related by the 'conservation-of-energy' constraint;

$$\alpha_\lambda + \rho_\lambda + \tau_\lambda = 1 \quad . \qquad \text{(C-2)}$$

It is not immediately obvious that the usual form of Kirchhoff's law can be used here (i.e., that the emissivity ($\varepsilon_\lambda$) can be substituted for the absorptance ($\alpha_\lambda$) in Equation C-2), because the quartz envelope is a partially transparent reflecting body. Rigorous calculations have shown, however, that this procedure is valid

here, if the transmittance ($\tau_\lambda$) and the reflectance ($\rho_\lambda$) are redefined to include all the effects of multiple scattering inside the quartz.[57] Equation C-2 may therefore be used to determine ($\varepsilon_\lambda$) from published data for $\rho_\lambda$ and $\tau_\lambda$.[51,52] The average values of ($\rho_\lambda$) which were used in this equation are summarized in the legend in Figure 8. Note that the high temperature of the quartz will undoubtedly wash out the broad minima due to reststrahlen phenomena. But the curves in Figure 8 show that our final conclusions would remain unchanged, even if the emissivity of the quartz were unity throughout the entire thermal-infrared spectral region.

Now let us consider the primary source of heat to the quartz envelope. First of all, note that the spectral range between 0.2 and 4μm contains approximately 99% of the total energy radiated from a blackbody at a temperature of 6000°K. As noted in the previous section, the 20-kW lamp radiates ∿50% of the total input power. It therefore follows that ∿1-kW is absorbed as the radiation from the arc passes though the quartz. Conduction should serve as a heat sink and not a source of heat for the quartz, because the liquid cooled electrodes are kept at a temperature of 450°C.[48] Convection by the xenon-gas is, however, a source of heat to the quartz. Nevertheless, as a first order solution to this problem, both conductive and convective modes of heat-transfer from and to the quartz will be neglected. Let us therefore estimate the approximate temperature of the quartz by assuming that it is a sphere which radiates 1-kW of power. This temperature can be obtained by solving the

following integral equation:

$$\pi A \int_0^\infty \varepsilon_\lambda N_\lambda(T)\, d\lambda \approx 10^3 \qquad \text{Watts,} \qquad \text{C-3}$$

where $N_\lambda(T)$ is the Planck blackbody function in units of Watts-$cm^{-2}$-$ster^{-1}$-$\mu m^{-1}$, and $\varepsilon_\lambda$ is the spectral emissivity. The total radiating surface area is denoted by (A), and $\pi$ is the average hemispherical solid angle for each surface element of a Lambertian emitter. The tables in Reference 22 were used to solve this equation for the temperature (T). After three trial-and-error iterations, the approximate solution was found to be $T \approx 1430°K$. If Equation C-3 is solved with the emissivity set equal to unity, then the solution is $T = 1080°K$.

The value used for the power radiated by the quartz in Equation C-3 (i.e., 1-kW) is based on a very crude approximation. Therefore the final radiance calculations were made with a very conservative upper limit for the temperature (i.e., $T = 1800°K$), which is set by the softening temperature of quartz. (31)

Verification of the Searchlight Intensity Equation

In Section 3.2, it was shown that the spectral radiant intensity in the searchlight beam is given by Equation 11, which is:

$$J_\lambda = \frac{9}{2}\pi f^2 N_\lambda(T) \qquad \text{Watts-ster}^{-1}\text{-}\mu m^{-1}, \qquad \text{(C-4)}$$

where (f) is the focal length of the reflector and $N_\lambda(T)$ is the Planck blackbody function at temperature (T). We can make a pragmatic check on whether this equation is reasonable by using it to calculate the searchlight brightness in the visible spectral range. The result should at least be the same order of magnitude as the reported performance of a minimum brightness capability of $\sim 8 \times 10^8$ candlepower in a beam width of $\sim 1.5°$.[47] In order to convert $J_\lambda$ in Equation C-4 into equivalent candlepower (i.e., lumens-ster$^{-1}$), we must integrate over the visible response function of the eye, as in Equation C-1. The result of this calculation is a brightness of $9.8 \times 10^8$ lumens-ster$^{-1}$. Over the visible spectral range, the transmission of the quartz is $\sim 93\%$,[21] and the reflectivity of the reflector is $\sim 80\%$.[47] Multiplication by these factors reduce the brightness to $\sim 7.3 \times 10^8$ candlepower. This brightness, which represents the average value over the beam solid-angle, is very close to the reported value of minimum <u>peak</u> beam candle power (i.e., $\sim 8 \times 10^8$).[47]

The average beam divergence may be roughly approximated as follows. A spherical blackbody at a temperature of 6000°K must have a radius (r) of 3.3mm in order to have a surface large enough to radiate 10-kW. From figure 10, it follows that the half-angle ($\alpha$) of the beam divergence cone at infinity is:

$$\alpha \approx r/\ell \qquad (C\text{-}5)$$

where $\ell$ is the average source to reflector distance, and is approximately equal to 3/2 times the focal length. Evaluation of Equation C-5 gives a value of $\sim 0.7°$ for ($\alpha$), with a corresponding full beam width of $\sim 1.4°$. This result was obtained with the aid of some very rough approximations and the remarkable agreement with the reported beamwidth (i.e., 1.5°) is undoubtedly somewhat fortuitous.

A particularly interesting aspect of Equation C-4 is that the beam intensity is independent of the total power radiated by the source. Note that the temperature of a blackbody source determines the minimum surface area required to radiate at any given power level. For a source of area (A), this relation is given by the Stefan - Boltzmann Law:

$$P = \pi A \int_0^\infty N_\lambda(T)\,d\lambda = A\,\sigma\,T^4 \qquad \text{Watts} \qquad \text{(C-6)}$$

where $N_\lambda(T)$ is the Planck blackbody spectrum, and the Stefan-Boltzmann constant ($\sigma$) is equal to $(5.6697 \pm 0.0029) \times 10^{-12}$ Watts $cm^{-2}$ $°K^{-4}$.[21] For a spherical source of radius (r), Equations C-5 and C-6 give the relationships between the total power radiated at temperature (T) and the beam divergence ($\alpha$). Increasing the power level at constant temperature merely increases the beam divergence ($\alpha$). Note that one of the consequences of the Second Law of Thermodynamics[58] is that radiation from a finite source at temperature (T) cannot be

focused, with passive optics, into a region small enough to produce an equilibrium temperature greater than (T). It follows that Equation C-4 is consistent with this law.

## APPENDIX D

### SOME FUNDAMENTALS OF DETECTION SYSTEM SENSITIVITIES

In this appendix the threshold sensitivities (NE$\Delta$T), NESR, and NE$\Delta\rho$ of the spectrometer are expressed in terms of some of the fundamental parameters of the system. Available information concerning the values of these parameters have been used to reconfirm the estimated value of NE$\Delta$T $\sim$ 1°K which was referred to in the main text. (5)

Consider the change in spectral power $\delta P_\lambda(\theta)$ registered by the optical system of S-191, due to a temperature change ($\delta$T) of a surface target at temperature (T) which is viewed at an angle ($\theta$) from nadir. From Equation 12, the expression for this spectral power change is:

$$\delta P_\lambda(\theta) = \tau_\lambda(\theta)\, A_c \Omega_s \frac{\partial N_\lambda(T)}{\partial T} (\delta T)\eta \quad \text{Watts-}\mu\text{m}^{-1}, \qquad \text{(D-1)}$$

where $\tau_\lambda$ is the spectral transmission along the atmospheric path-length R($\theta$). The area of the instrument collection aperture is $A_c$; the Planck blackbody spectral function is $N_\lambda(T)$ Watts-cm$^{-2}$-ster$^{-1}$-$\mu$m$^{-1}$; and $\eta$ is the efficiency of the optical system. The solid angle which the target area subtends at the detector is represented by:

$$\Omega_s \equiv A_s(\theta)\cos\theta/R^2 \text{ ster.} \qquad \text{(D-2)}$$

In Equation D-1, it has also been assumed that the surface emissivity of the target is unity, and that this emissivity is independent of temperature.

Let us next consider the rms noise power from a detector, with an effective sensitive area ($A_d$) and a bandwidth ($\Delta f$). By definition, this is equal to the noise-equivalent-power of the detector:[21,59]

$$\delta P_n \equiv (A_d \Delta f)^{1/2}/D^* \quad \text{Watts}, \tag{D-3}$$

where D* is the normalized detectivity in units of (cm $Hz^{1/2}$ $Watt^{-1}$). This detectivity (D*) represents the detector responsivity (in units of volts/watt) divided by the rms noise voltage, and then normalized to remove the dependence on surface area and bandwidth.[59] The formula represented by Equation D-3 is based on the assumption that the overall system is detector-noise-limited. This is usually a valid assumption in the infrared spectral region.[60] However, a completely rigorous analysis requires detailed consideration of noise from the pre-amplifier and amplifier signal processing systems, and performance degradation due to the finite response time of the system.[61]

The signal to noise ratio can now be evaluated in terms of the results from Equations D-1 and D-3:[60]

$$S/N = \eta'(\delta P_\lambda \delta\lambda)/(\delta P_n), \tag{D-4}$$

where $\eta'$ is the efficiency factor for conversion of the input signal from peak-to-peak to the corresponding rms value. Note that the input signal is chopped on-and-off (i.e., amplitude modulated) before it is spectrally analyzed so that calibration sources can be viewed at regular intervals.[4] Substituting the previous results for the factors in Equation D-4, we obtain:

$$S/N = \eta\eta' \tau_\lambda A_c \Omega_s D^* \frac{\partial N_\lambda(T)}{\partial T} (\delta T)(\delta\lambda)/(\Delta f A_d)^{1/2} \qquad (D\text{-}5)$$

The temperature change ($\delta T$) is defined as the noise-equivalent-temperature-difference (NE$\Delta$T) when the signal to noise ratio is equal to unity. Therefore, it follows that:

$$NE\Delta T = (A_d \Delta f)^{1/2} \Big/ [\eta\eta' \tau_\lambda A_c \Omega_s D^* \frac{\partial N_\lambda(T)}{\partial T} \delta\lambda] \quad °K. \qquad (D\text{-}6)$$

Alternatively, the noise-equivalent-radiance (NER)[45] may be expressed as:

$$NER = \frac{\partial N_\lambda(T)}{\partial T} NE\Delta T \quad \text{Watts-cm}^{-2}\text{-ster}^{-1}\text{-}\mu\text{m}^{-1} \qquad (D\text{-}7)$$

Also note that NER or NESR (i.e., noise-equivalent-spectral-radiance) may be defined in terms of the detector characteristics, via Equation D-3.

Equation D-6 may be further simplified by noting that the following invariant relation holds for a well designed optical system:[45]

$$\Omega_s A_c = \Omega A_d \quad , \qquad (D\text{-}8)$$

where $\Omega_s$ is the solid angle which the source area ($A_s$) subtends at the collector area ($A_c$); and $\Omega$ is the effective solid angle for convergence of radiation onto the detector area ($A_d$). The validity of this relation is easily proven by noting the following equality for an optical system with a fixed solid angle field-of-view ($\Omega_s$), and an effective focal length (f):

$$\Omega_s = A_s \cos\theta/R^2 = A_d/f^2 \quad , \qquad (D\text{-}9)$$

where ($\theta$) is the off-vertical viewing angle; the source to collector distance is (R); and the effective focal length (f) is equal to the collector to detector distance. Multiplication of both sides of this last Equation by the collector area ($A_c$) yields Equation D-8, where

$$\Omega \equiv A_c/f^2 \quad \text{ster} \quad . \tag{D-10}$$

Substitution of Equation D-8 into Equation D-6 yields:

$$NE\Delta T = (\Delta f)^{1/2} / \left[\eta\eta'\tau_\lambda\ \Omega A_d^{1/2}\ D^*\ \frac{\partial N_\lambda(T)}{\partial T}\ \delta\lambda\right]. \tag{D-11}$$

Evaluation of this expression, on the basis of information available to this author[4,5,21] concerning the relevant parameters for S-191, yields a value of $\sim$1°K for NE$\Delta$T, at a wavelength of $\lambda$ = 10 $\mu$m. This is in very good agreement with the value inferred from the noise-equivalent-radiance curve for S-191 in Reference 5.

Note that Equation D-1 may be generalized to include variations in received power due to changes in the surface reflectance of the incident flux of power from the sun. The additional contribution to the spectral power received by the detector is:

$$\delta P'_\lambda = \tau_\lambda(\theta)\frac{A_c}{A_s}\left(\frac{\Omega_s}{\pi}\right)\eta\ \left[\tau'_\lambda(\theta_\odot)\ A^p_\odot\ \Omega_e(\theta_\odot)N_\lambda(T_\odot)\delta\rho(\theta,\theta_\odot,\Phi_\odot)\right] \tag{D-12}$$

Watts/$\mu$m,

where the coefficients which were not defined for Equation D-1 are: (a) the atmospheric transmission $\tau'_\lambda(\theta_\odot)$ along the line-of-sight path between the sun and the surface target on Earth; (b) the angle $(\theta_\odot)$, which this solar path makes with the local vertical at the Earth; (c) the solid-angle which the target area $A_s$ subtends at the sun (i.e., $\Omega_e = A_s \cos(\theta_\odot)/R_\odot^2$), where $R_\odot$ represents the distance between the sun and the Earth; and (d) $A_\odot^p$, the projected area of the sun (i.e., $A_\odot^p = \pi r_\odot^2$), where $r_\odot$ is the solar radius. The spectral emittance of the sun is represented by the Planck function $N_\lambda(T_\odot)$ at a temperature of $T_\odot \approx 6000°K$. And finally, the differential change in surface reflectance is represented by $\delta\rho(\Theta, \Theta_\odot, \Phi_\odot)$, which is a function of the observation-angle $\Theta$, the sun-angle $\Theta_\odot$, and the azimuthal angle $\Phi_\odot$ between the plane of incidence and the plane of reflectance. For wavelengths less than $\sim$4 μm, the spectral intensity of radiation emitted from the surface of the Earth is more than an order of magnitude less than that received at Earth from the sun.[2] In this spectral region, the differential reflectance may be defined as NEΔρ (i.e., noise-equivalent-reflectance-difference) for conditions analagous to those used to define NEΔT via Equations D-1 through D-6.